A 3D panel method code for the analysis of swept wind turbine blade geometries

Comparison to lifting line simulation

Sorin Seremet

Master of Science Thesis

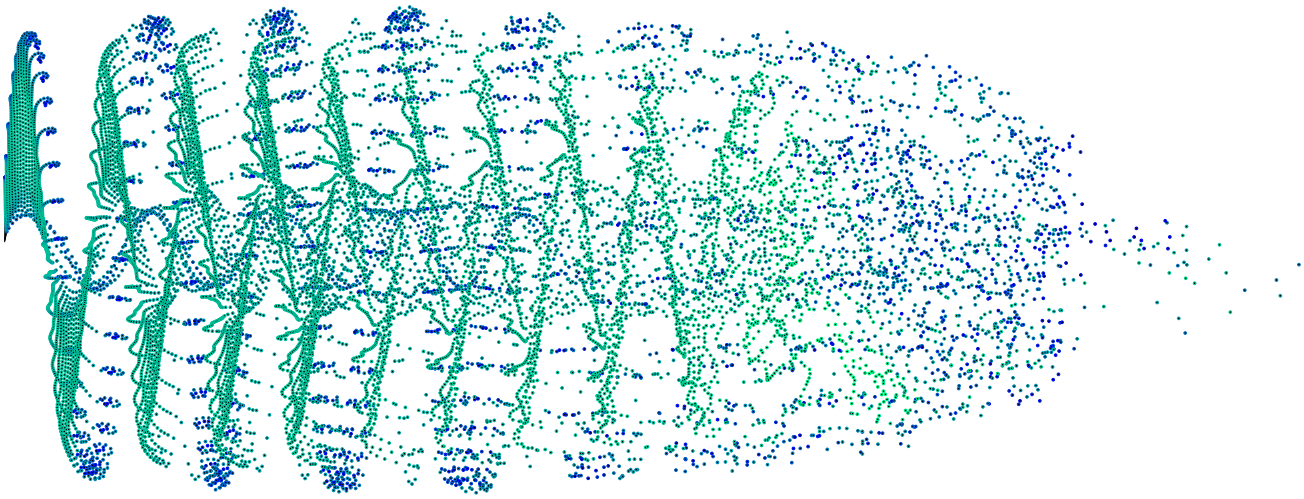

TU Delft Delft University of Technology

Flow Physics and Technology

A 3D panel method code for the analysis of swept wind turbine blade geometries

Comparison to lifting line simulation

Master of Science Thesis

For the degree of Master of Science in Aerospace Engineering at Delft University of Technology

Sorin Seremet

August 24, 2023

Faculty of Aerospace Engineering (AE) · Delft University of Technology

The work in this thesis was supported by TNO (Netherlands Organisation for Applied Scientific Research). Their cooperation is hereby gratefully acknowledged.

Delft University of Technology
Department of
Flow Physics and Technology

The undersigned hereby certify that they have read and recommend to the Faculty of Aerospace Engineering (AE) for acceptance a thesis entitled

A 3D panel method code for the analysis of swept wind turbine blade geometries

by

Sorin Seremet

in partial fulfillment of the requirements for the degree of

Master of Science Aerodynamics & Wind Energy

Supervisor(s):

Prof.Dr.ir. Carlos.Simão Ferreira

Reader(s):

Dr.ir. Alexander van Zuijlen

Dr. Wei Yu

Abstract

A 3D panel method code, named AWSM3D, is developed as an extension to the AeroModule aerodynamic software suite of TNO which includes a Blade Element Momentum theory (BEM) and a Lifting Line (LL) code. The underlying panel code method is presented along with a gradual process of simulation validation culminating in validating the code against the New MEXICO experimental dataset and an established panel code. In view of exploring the avenue of sweeping wind turbine blades as a way of increasing wind turbine efficiency, the capabilities of the three proposed aerodynamic models in solving flows about swept geometries are studied. The unmodified BEM model is incapable of adequately modeling flows over swept geometries. The limits of the cross-flow theory which the LL simulation hinges on for the simulation of swept flows are put to the test. Both a fixed wing and a conventional Horizontal Axis Wind Turbine case show that the LL solution in proximity to body extremities where the cross-flow component is prominent fails to capture smaller-scale local effects caused by said cross-flow. Despite this, the larger-scale effect is reproduced well. Although AWSM3D requires no airfoil polars and produces an accurate inviscid flow solution for more complex body geometries, it currently excludes viscosity and has a much higher computation time in comparison to an LL. A number of further AWSM3D development and research into the effects of sweep suggestions are formulated.

Table of Contents

List of Figures

List of Tables

Acknowledgements

As I reflect upon completing this Master's thesis, I am filled with a profound sense of gratitude for the multitude of individuals who have contributed to my academic journey. It is with great pleasure and humility that I express my heartfelt appreciation to all those who have supported and guided me along the way.

First and foremost, I am indebted to my supervisors from TNO, Koen Boorsma and Erik Fritz, for their guidance, expertise, and unwavering support. Their invaluable insights, constructive feedback, and continuous encouragement played a pivotal role in shaping this research. I am truly grateful for their patience, dedication, and commitment to my academic growth. The astute remarks we made on our cultural differences will be remembered fondly. Erik is easily the unsung hero of this thesis; his meticulous attention to detail, lightning-fast decision-making and capability to understand my thoughts before I could have produced massive advances for this work. It is not in the single digits already how many times you have over exceeded your duties as a supervisor to lend me a much needed hand of help.

I would also like to extend my most profound appreciation to my supervisor from TU Delft, Prof. Dr. ir. Carlos Simão Ferreira. Your guidance and mentoring helped me tremendously in structuring my thesis efforts, and your valuable input has undoubtedly strengthened the outcomes of this thesis. I can decisively say that your professionalism, inspiring teaching style and passion for aerodynamics have been the main reason for me to pursue this field of work at TNO.

I am grateful to the supporting staff of TNO for making my (re-)onboarding and time spent working hassle-free. Thanks to André Pinto Ribeiro for sharing valuable panel code know-how. Many thanks to Vadim Uritsky for his help setting up the mesh generator. Thanks to Dr. ir. Arne van Garrel for the courtesy of providing panel code simulation results for validation and for having devised the original AWSM software in such a concise and flexible manner.

In addition, I would like to express my heartfelt thanks to my friends and family for their support, love, and belief in my abilities. Their presence, whether near or far, has provided a sense of comfort and reassurance.

Finally, I would like to express my deep gratitude to the Netherlands for being the hosting country of my Master's degree journey. I am immensely grateful for the rich cultural experiences and personal growth that this country has afforded me.

Chapter 1

Introduction

In recent years, modern wind turbines have surpassed the 10 MW threshold. This ever-growing power output per turbine is largely realized by increasing the area swept by the rotor. Two consequences of this trend are:

1. The analysis of the turbines aeroelastic behavior becomes increasingly important and requires physically accurate numerical tools.
2. Techniques need to be found with which this aeroelastic behavior of wind turbine blades can be tailored.

In this thesis, swept blade geometries will be analyzed. Blade sweep, resulting from a blade axis curved in the rotor plane, is an aeroelastic tailoring technique used to couple bending and twisting deformations. This bend-twist-coupling can then be used to passively alleviate loads, which may lead to more efficient wind turbines. As such, that may drive the Levelized Cost of Electricity (LCOE) of wind energy down, creating the conditions for a higher fraction of renewable sources in the energy market. Aerodynamically, the curved blade results in changes in the induction system as well as in the inflow conditions. Especially around a swept blade tip, crossflow over the airfoil sections will occur. It is expected, that the accuracy with which such effects can be represented largely depends on the fidelity of the simulation tool. Thus, the goal of this thesis is the identification of shortcomings and benefits of using simulation methods of three fidelities, namely BEM, lifting line formulation, and panel method.

1-1 Research question, objectives and sub-goals

Below the research questions that the thesis aims to address are formulated. These have been identified based on the current scientific body of knowledge regarding blade sweep effects. The particular gap in knowledge targeted deals with the lack of aerodynamic analysis tools well suited for swept blade geometries.

1-1-1 Research questions

The following research questions are proposed:

1. Is 2D blade element theory still valid for a swept blade, and what parameters limit the validity?
   (a) What are the observed differences between the 3D panel surface simulation and the lifting line simulation?

   (b) Can these differences be corrected at the airfoil level?
2. What is sufficient validation of a 3D panel model for the swept blade configuration?

The answers to these questions shall grant a deeper understanding of the physical phenomena that aerodynamic models shall be able to capture in order to accurately resolve the effects of sweep.

1-1-2 Research objective

The main objectives of the research are:

Analyze the aerodynamic implications of a swept blade geometry by using a 3D panel method. The latter has to be developed first.
Establish whether a lifting line model can be adjusted to ensure adequate modeling of sweep effects.

1-2 Theoretical content/methodology

The first step is to produce an unsteady 3D panel method model with a free wake module. The latter is readily available already in the AeroModule, coupled with the lifting line based (AWSM) aerodynamic model. The theoretical basis of the 3D panel method lies in potential flow theory. The numerical implementation follows from the discretization of the blade geometry and of the potential flow governing equations. The algorithm for the setup of the panel method follows closely the approach detailed in [5]. The following breakdown is proposed:

1. Implementation of a 3D panel surface model in TNOs AeroModule.
   (a) The simulation tool AeroModule, developed in-house by TNO, currently consists of a BEM formulation and a lifting line implementation (AWSM) to simulate the aerodynamic performance of a wind turbine rotor. AeroModule can be run as standalone executable or coupled to structural solvers such as Phatas or SimPack. As part of this master thesis project, the capabilities of AeroModule will be extended by altering the vorticity-based solver AWSM. Additionally to the lifting line formulation currently available, a three-dimensional surface panel distribution will be implemented to represent the blade. Commonly known as a panel method, such a code gives more detailed insight into the load distribution on the blade's surface. The free wake formulation already existing within AWSM can then be combined with the panel method to extend AeroModule to a higher fidelity level.
   (b) The model will be validated.
2. Simulating a reference straight and swept configuration. For this purpose, the IEA 15 MW reference rotor blade definition shall be used ([12]). This will be simulated with the 3D panel model and lifting line. As a follow-up, an analysis will be performed in order to answer the research questions. This shall mainly result from comparisons between the results obtained from the two models used.

1-3 Project description

This thesis represents a collaboration between TU Delft and the wind energy research group within the Energy Transition unit of TNO. Most programming endeavors will be performed in the protected environment of TNO, which is to be accessed via a laptop provided by TNO.

The intent is to further develop AeroModule, an in-house software suite developed by TNO and capable of running state-of-the-art aerodynamic analysis, as presented in [1]. For the scope of this work, the stand-alone version shall be employed, i.e. uncoupled from the structural solver. The current version of AeroModule contains a vorticity-based flow solver based on a lifting line algorithm called AWSM, which shall be used whenever lifting line simulation results are needed. The programming language used is free-form Fortran, compiled using Intel® Fortran Compiler.

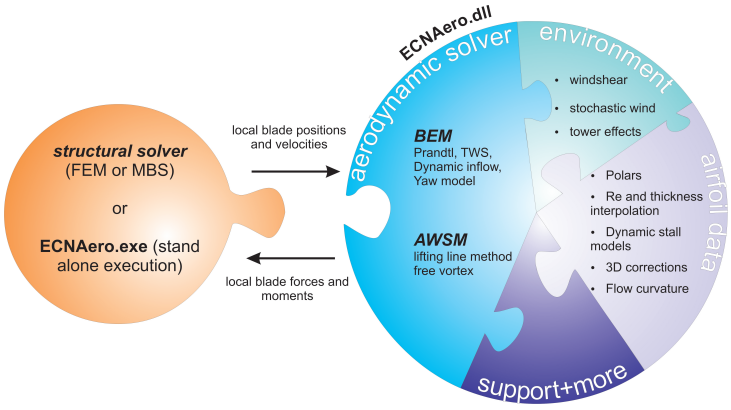

Figure 1-1: AeroModule overview, reproduced from [1].

In its current form, AWSM is based on generalized lifting line theory using a nonlinear solution approach. The latter is needed to incorporate the effects of viscosity by means of supplying aerodynamic airfoil polars. In this manner, the flow solution is obtained once equilibrium is reached between the strength of the lifting line potential flow elements and strip element forces, as dictated by the section aerodynamic properties. The wake is modeled as a free wake discretized in vortex rings, as shown in Figure 3-8.

1-4 Results, outcome and relevance

The desired outcome of the thesis work is to validate a 3D panel method for the analysis of swept blade geometries. The innate capability of panel methods to better represent complex geometries as compared to lifting line models shall be put to the test. An investigation into the possibility of applying correction factors to lifting line models to correct for cross-flow or other factors shall be launched once the comparison of the results is performed. The accuracy of the models shall be quantified by inspecting the pressure distributions on the surface, velocity, circulation, and loading.

The proposed research goal of this thesis work is to fill the gap in knowledge with regard to the suitability of aerodynamic models such as lifting line or panel method models for the analysis of flows around swept geometry blades. Aerodynamically, the swept blade geometry induces changes in the induction system as well as in the inflow conditions. Lifting line codes commonly rely on sectional viscous aerodynamic data, which disregard the effects of cross-flow. Elementary panel methods are not affected by this limitation; however, viscous effects are not included. The solution follows directly from the governing equations of potential flow, which neglect viscosity. Boundary layer models would be needed to incorporate the modeling of viscous effects. The current analysis steers clear of viscous effects by means of adapting the lifting line for an inviscid solution. The outcome of this thesis is a valid tool for analyzing swept blades, which is needed for the design of advanced rotor blades that exploit bend-twist coupling to passively alleviate structural loads.

Chapter 2

Effect of blade sweep

This chapter provides an overview of past research directed at the aerodynamics of swept geometries. First, older studies concerning fixed wing aerodynamics are explored in section 2-1. As a follow-up, an overview of recent research into applications of sweep for wind turbine blades is presented in section 2-2.

2-1 Cross-flow principle

The books of Hoerner provide a compilation of studies done throughout the 20th century involving swept fixed wing cases and present a consolidated and unified theory coined the cross-flow principle [2, 13] (or simple sweep theory [14]). An illustration is given in Figure 2-1 for the case of a wing subjected to a yawed inflow. The basic premise of this theory is summarized here. According to cross-flow theory, the u velocity component which is parallel to the wing axis has no influence on pressure forces and may therefore be neglected. Reconstructing the lift force equation given the resulting implications yields the following relation:

$$L \propto \alpha_n w^2 \propto \left(\frac{1}{\cos\lambda}\right)\cos^2\lambda \propto \cos\lambda \tag{2-1}$$

, where L is the lift force, α_n is the angle of attack in the plane of the wing section, w is the component of velocity parallel to the chord line, and λ is the sweep angle.

In essence, the cross-flow principle represents a 2D correction for flows around swept geometries. It does not account for the influence of the wake and therefore does not provide insight into the interactions of the bound circulation with the wake, which represents a 3D flow pattern of importance around wing or turbine blade tips. This becomes even more of an imperative once sweep is introduced. Nonetheless, this result seemed to resonate quite well with experimental measurements, especially regarding the total or average lift generated by swept wings [15].

Another perspective on this matter is presented by Kuchemann [3]. The airfoil is represented as a series of source line elements distributed along its chordline and extending to infinity in the direction normal to the free stream. For small thickness/chord ratios ($t/c \leq 20\%$) it is approximated that the pressure coefficient c_p is proportional to the (t/c) ratio. Schematics of the flow pattern over a swept wing are shown in Figure 2-2. Recognizing that the streamlines roughly follow the contour of the sheared wing of infinite span along the incoming flow direction, it is clear that the c_p will be adjusted accordingly to account for variation in (t/c).

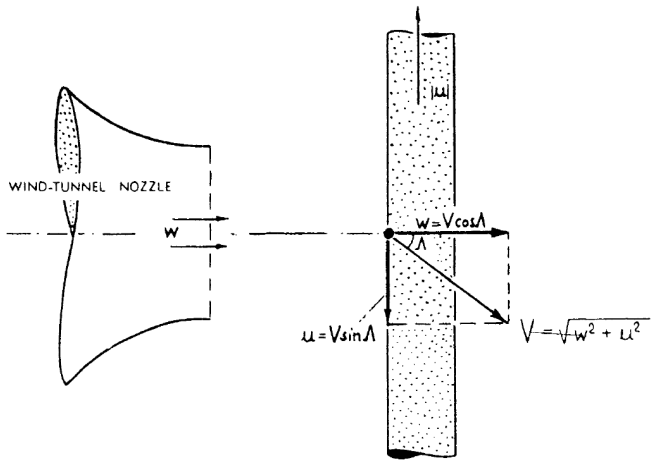

Figure 2-1: Swept flow decomposition, reproduced from [2].

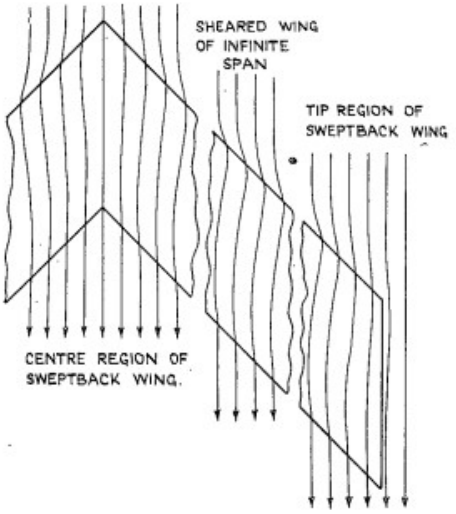

Figure 2-2: Flow patterns over swept geometries, reproduced from [3].

2-2 Wind turbine applications

The effect of wind turbine blade sweep has been thoroughly studied to verify the hypothesis that appropriate blade sweep can drive the cost efficiency and performance of wind turbines up. The main mechanism behind this improvement lies in introducing aeroelastic bend-twist coupling, which is sought after as a method of passive load alleviation. The idea is that by means of sweeping the blade aft, the aerodynamic axis is also shifted aft of the elastic axis, which leads to the blade having a tendency to twist towards feather as loading increases, thereby lowering the angle of attack, and by extension, the loading. Therefore, it confers the blade static stability in case of a gust.

This concept was first set forward for wind turbine applications by Liebst [16]. For the proposed parabolic blade curvature, a quasi-steady aerodynamic model and simple beam theory linearly superimposing torsion and bending were used. Liebst concluded that a moderate tip deflection and flapwise bending moment reduction were achieved in response to a gust for a typical blade structure. However, a much more promising result was obtained once the torsional rigidity of the blade was greatly reduced. The author emphasized the importance of low torsional and high flexural rigidities for effective use of sweep.

Zuteck [17] picked up on the work of Liebst. A circular sweep shape was quickly dismissed by the author due to poor induced twist distribution along the blade. To proceed, the author introduced a

power law curve to improve on the sweep shape, along the lines of Equation 2-2:

$$y = y_{tip}\left(\frac{x - x_{start}}{L_{Blade} - x_{start}}\right)^{\gamma} \tag{2-2}$$

, where y is the distance from the pitch axis to the sweep curve, y_{tip} is the respective distance at the blade tip, L_{Blade} is the blade length, γ is the exponent of the power law curve, and x is the distance from the root along the unswept blade, with x_{start} denoting the radial position starting from which this relationship is applied to obtain the swept profile. A graphic representation is given in Figure 2-3, where d_{tip} replaced the y_{tip} in Equation 2-2.

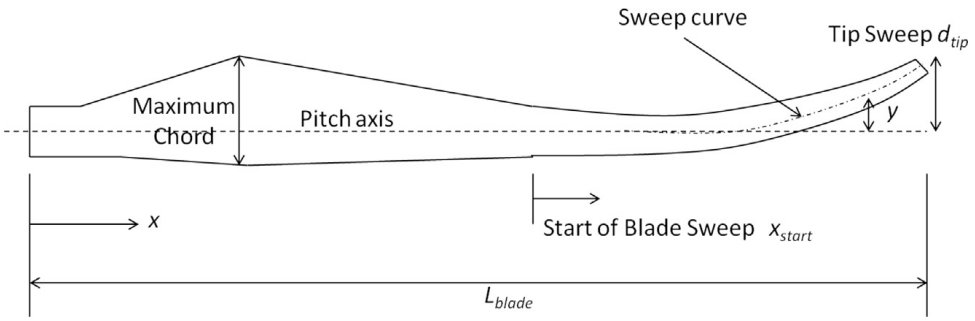

Figure 2-3: Swept blade definition, reproduced from [4].

Using the 30 m Sandia blade as a baseline [18], Zuteck held an analysis for a 1 m tip deflection and an exponent of 4 describing the sweep distribution. It was found that a substantial twist of 4 degrees at the tip could be produced, or even 7 degrees if torsional rigidity is decreased by means of a reduction of blade thickness, all for a load case resembling a steady 1 MW power production. Earlier findings of Liebst are reinforced here again as blade sweep is believed to be able to pave the way towards lower costs of energy by allowing for more energy efficient blades. This is mainly due to lower structural stresses and lower fatigue damage.

Joined by Zuteck, Larwood [19] took into consideration the Zond Z-50 wind turbine as a base for the development of the Sweep Twist Adaptive Rotor (STAR) blade. The performance of the original 50 m blade was then compared to the 56 m STAR rotor with 2.2 m tip displacement, called STAR6, and a 56 m straight version of STAR6, called BASE6. The analysis was run using NREL's FAST and MSC's ADAMS simulation tools. It was established that the peak flapwise moments were 20% lower for the swept blade compared to the straight blade, but still a little higher than the shorter baseline blade. Nonetheless, this was accompanied by a 5–10% increase in power production.

The last publication surrounding the STAR rotor is by Ashwill [20]. The STAR6 blade was revamped into STAR7, starting from a Zond 750 turbine baseline and employing a series of airfoils specially designed for it. Showing favorable results when compared to the baseline Zond 750 using FAST and ADAMS tools, a revised version of the rotor went into production, under the STAR 54 denomination. The blades spanned 26.1 m with a 54 m rotor diameter and were placed on a Zond 750 turbine, which originally came equipped with 23.5 m long blades and a 48 m rotor diameter. Strain gauges were placed close to the root to measure bending moments while the turbine was operating on an IEC Class II test site in California. Measurements indicated that the bending moments of the longer STAR 54 blade were comparable to the straight baseline Z48 blade, whereas without the inclusion of sweep the longer blade was expected to experience an 80% increase in bending moments. Overall, the STAR rotor was found to produce 10–12% more power on average as compared to the Z48 baseline rotor.

Chattot [21] used a vortex model based on the Goldstein approach with a frozen wake model to study the effects of sweep, among others, on the aerodynamic properties of the blade. Both a forward and

a backward sweep of 10% was applied on top of the baseline NREL 20 kW rotor defined in [22]. The sweep itself was obtained by a shearing transformation of the blade, wherein the sectional chord orientation in the swept region stayed parallel to the blade root chord. Comparing the simulation results for operation at 6 kW power for the three considered cases revealed that the rotor efficiency of the backward swept blade went up to $\eta = 0.377$ from the baseline version which had $\eta = 0.375$, whereas the forward sweep caused a slight decrease in rotor efficiency. As expected, the pitching moment varied as well, with the forward swept blade having the least nose-down pitching moment and the backward swept one having the largest pitching moment. The author also recognizes that the wake shape is altered as the strong tip vortex is shed further away from the rest of the blade if sweep is applied.

Suzuki *et al.* [23] followed up on the work of Chattot by refining the aerodynamic analysis. A hybrid method was used whereby a CFD solver was used in a region around the blade and the far-field was resolved using a vortex model with a frozen wake. The study confirmed earlier findings by observing an increase in pitching moment for the backward swept blade and an efficiency gain smaller than 1% for the same test blade and operating conditions. An additional analysis was performed on the swept blade which underwent an optimization of the twist and chord distribution for the same thrust force on the tower. This time the efficiency rose by 2.64%.

Verelst *et al.* [24] performed a similar analysis on the larger 5 MW NREL reference rotor [25] using the HAWC2 aeroelastic simulation tool. The 126 m diameter baseline rotor was analyzed for combinations of sweep parameters ranging from -6 m to 6 m for tip deflection and exponents of the power law curve in the 1–5 range, exposed to turbulent free stream velocities from 4–26 m/s, amounting to 1452 cases in total. The HAWC2 simulation was set up such that cross-flow is neglected. Judging from the results, the forward sweep was deemed the least favorable, causing instabilities upwards of 3 m tip deflection, which is also reflected in the increased root bending moment fatigue load for more moderate forward sweep. In agreement with previous papers, the backward sweep alleviated the flapwise bending moments. However, the power production was found to be lower than for the original blade layout, which was attributed to the sub-optimal geometric and aerodynamic design, which was initially optimized for the straight blade. It is suggested that a design optimization process involving torsional deformation should be employed in the design of a swept blade.

A study of a free yawing wind turbine with swept blades was conducted by Picot *et al.* [26]. For this study, a 100 kW stall-controlled rotor with a 21 m diameter was selected as a baseline for applying a sweep with a tip deflection of 1.2 m and an exponent of 4 for the power law curve. Using the HAWC2 tool, the pitching moment was established to increase under a higher blade loading for the swept case, contributing to the twist-to-feather motion. As opposed to Verelst, backward sweep was said to increase the rated power of the rotor.

Efforts to scale up and capitalize on the validated design of the STAR rotor were undertaken by Larwood *et al.* [4]. The rotors considered in this study are the STAR7 rotor and designs for 1.5, 3, and 5 MW rotors derived from the WindPACT study [27] and the latter being the 5 MW NREL reference blade [25]. These were subsequently analyzed using an extension of FAST capable of modeling swept blade kinematics and aerodynamics, called CurveFAST. First, CurveFAST was validated using measurement data collected from the field tests of STAR7, after which it is used for a parametric study of the effects of varying torsional stiffness, tip deflection and curve exponent. After applying sweep to the baseline blades, the Betz method was used to optimize the design of the blade planform. The results of the simulations showed that the flapwise bending moment exhibited the highest sensitivity to the tip deflection parameter. For STAR7, the largest energy production was obtained for the case when the blade resembled a straight blade the most. For the 1.5 and 3 MW swept blades, there was a 5% increase in energy production mainly due to the larger rotor radius with respect to the baseline versions. The flapwise bending moments showed a decreasing trend at the expense of a slight edgewise bending moment increase. The 5 MW rotor showed twist

instability even for small tip sweep which is suspected to be caused by flutter instability.

A larger focus on the aerodynamics of swept blades was present in the study of Li *et al.* [28]. The paper refers to the implications of sweep in the form of changing the location where the vorticity is shed from the blade and therefore modifying the induction system of the blade. Secondly, the vortex filaments describing the bound vorticity change orientation and distance to the rest of the blade, thus changing the induced velocities.

Chapter 3

Free Vortex Models

Vortex models are tools used to solve the aerodynamics of the flow over a body, rooted in potential flow theory. These take an intermediate spot between Blade Element Momentum (BEM) and Computation Fluid Dynamics (CFD) models both in terms of solution fidelity and computational complexity.

3-1 Potential flow theory

The theoretical foundation of potential flow theory lies in the Navier-Stokes equations, listed below in differential form:

$$\vec{\nabla} \cdot (\rho \vec{u}) = 0 \qquad \text{Conservation of mass} \qquad (3\text{-}1)$$

$$\frac{\partial(\rho \vec{u})}{\partial t} + \vec{\nabla} \cdot \rho \vec{u} \otimes \vec{u} = -\vec{\nabla} p + \vec{\nabla} \cdot \bar{\bar{\tau}} + \rho \vec{f} \qquad \text{Conservation of momentum} \qquad (3\text{-}2)$$

$$\frac{\partial(\rho e)}{\partial t} + \vec{\nabla} \cdot (\rho e + p)\vec{u} = \vec{\nabla} \cdot (\bar{\bar{\tau}} \cdot \vec{u}) + \rho \vec{f} \vec{u} + \vec{\nabla} \cdot \vec{q} + r \qquad \text{Conservation of energy} \qquad (3\text{-}3)$$

In order to simplify the solution process, a few limiting assumptions are formulated to narrow the scope of the solution and tone down the implementation and computational complexity. Neglecting compressibility, friction and heat transfer effects, the Navier-Stokes equations can be further simplified into the following form:

$$\vec{\nabla} \cdot \vec{u} = 0 \qquad (3\text{-}4)$$

$$\frac{\partial \vec{u}}{\partial t} + (\vec{u} \cdot \vec{\nabla})\vec{u} + \vec{\nabla} \frac{p}{\rho} = \vec{0} \qquad (3\text{-}5)$$

One last step conducive to formulating the basis of potential flow is to assume irrotational flow, i.e. $\boldsymbol{\nabla} \times \vec{u} = \vec{0}$. As such, the velocity can then be expressed as the gradient of a scalar potential Φ, such that:

$$\nabla \Phi = \vec{u} \qquad (3\text{-}6)$$

Combining Equation 3-6 with the continuity equation expressed in Equation 3-4 leads to the following expression, central to potential flow theory, referred to as the Laplace equation:

$$\nabla^2 \Phi = 0 \tag{3-7}$$

Equation 3-7 represents an elliptic partial differential equation that can be solved for a set of boundary conditions defined for a computational domain. By virtue of it being a linear differential equation, various valid solutions can be combined together using the superposition principle. The latter is a convenient tool that allows building up a general solution for fairly complex flows. By means of selecting the right combination of solutions, the entire set of constraints represented by the boundary conditions can be fulfilled in an elegant way.

Having resolved the velocity field, the loads and the pressure field can be obtained. Combining the velocity potential of Equation 3-6 with the Euler Equation 3-5 allows for the computation of the pressure, as per Equation 3-8. Further non-dimensionalizing this relationship by a reference velocity provides Equation 3-9 for obtaining the coefficient of pressure c_p.

$$\frac{p_{ref} - p}{\rho} = \frac{u^2}{2} - \frac{u_{ref}^2}{2} + \frac{\partial \Phi}{\partial t} \tag{3-8}$$

$$c_p = \frac{p - p_{ref}}{\frac{1}{2}\rho u_{ref}^2} = 1 - \frac{u^2}{u_{ref}^2} - \frac{2}{u_{ref}^2}\frac{\partial \Phi}{\partial t} \tag{3-9}$$

, where u stands for the local velocity magnitude and u_{ref} is a reference velocity used for the non-dimensionalization.

3-1-1 Solution based on Green's identity

The following solution method is based on the description included in Katz and Plotkin [5]. The computational domain for solving the Laplace equation is shown in Figure 3-1. A solid body with boundary S_B is submerged in a flow within a volume V enclosed by the outer boundary S_∞. The normal vector **n** is set such that it is oriented towards the exterior of the volume V both on S_B and S_∞. The problem at hand then requires solving the Laplace equation:

$$\nabla^2 \Phi = 0 \tag{3-10}$$

The first boundary condition arises from the physical constraint of flow non-entry through the impermeable surface of the solid. For a velocity potential expressed in the coordinate frame of the body, the following holds:

$$\nabla \Phi \cdot \mathbf{n} = 0 \tag{3-11}$$

Secondly, the effect of the body moving through the volume V should only have a local effect and vanish at infinity:

$$\lim_{\mathbf{r} \to \infty} (\nabla \Phi - \mathbf{v}) = 0 \tag{3-12}$$

, where $\mathbf{v}$ stands for the flow velocity as seen by the body and $\mathbf{r}$ stands for the position vector.

Suppose Φ_1 and Φ_2 are solutions of the Laplace equation. After performing vectorial manipulations and applying the divergence theorem, the following relation can be derived:

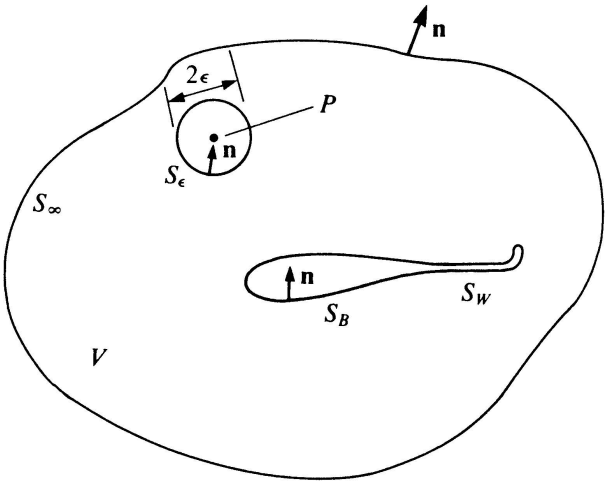

Figure 3-1: Potential flow problem domain, reproduced from [5].

$$\int_S (\Phi_1 \nabla \Phi_2 - \Phi_2 \nabla \Phi_1) \cdot \mathbf{n} dS = \int_V \left(\Phi_1 \nabla^2 \Phi_2 - \Phi_2 \nabla^2 \Phi_1 \right) dV \tag{3-13}$$

Suppose $\Phi_1 = \frac{1}{r}$ and $\Phi_2 = \Phi$, r being the distance away from point P in Figure 3-1. In this case, Φ_1 does satisfy the Laplace equation. Therefore, Equation 3-13 can be rewritten into:

$$\int_S \left(\frac{1}{r} \nabla \Phi - \Phi \nabla \frac{1}{r} \right) \cdot \mathbf{n} dS = 0 \tag{3-14}$$

Equation 3-14 holds when point P lays outside the volume V. The velocity becomes unbound as r tends to 0. In case it would be placed inside the computational volume, in order to reapply Equation 3-14, point P would have to be demarcated by a boundary S_ϵ corresponding to a small sphere centered at P. Expressing the same formula in spherical coordinates leads to the following expression:

$$-\int_{S_\epsilon} \left(\frac{1}{r} \frac{\partial \Phi}{\partial r} + \frac{\Phi}{r^2} \right) dS + \int_S \left(\frac{1}{r} \nabla \Phi - \Phi \nabla \frac{1}{r} \right) \cdot \mathbf{n} dS = 0 \tag{3-15}$$

By means of looking at the limiting case of the radius r of the sphere surrounding point P going to 0, evaluation of the first term in Equation 3-15 comes out as $-4\pi\Phi(P)$. Equation 3-15 can then be reconstructed as follows:

$$\Phi(P) = \frac{1}{4\pi} \int_S \left(\frac{1}{r} \nabla \Phi - \Phi \nabla \frac{1}{r} \right) \cdot \mathbf{n} dS \tag{3-16}$$

In case point P is moved to the boundary S_B, the first term of Equation 3-15 is evaluated for a hemisphere rather than a sphere. In that case, the potential changes by a factor 2:

$$\Phi(P) = \frac{1}{2\pi} \int_S \left(\frac{1}{r} \nabla \Phi - \Phi \nabla \frac{1}{r} \right) \cdot \mathbf{n} dS \tag{3-17}$$

Equation 3-17 is a powerful tool that expresses the potential field everywhere within V using information about Φ on the boundary S. It is largely responsible for the desirability of vortex models over BEM and CFD models. Whereas CFD requires computing the solution over the entire domain in order to get any result at all, vortex models only require solving for the boundary condition on the boundary surface itself, from which the rest of the domain solution can be reconstructed. At the same time, vortex models have higher fidelity than BEM models for a moderate computational effort increase.

3-1-2 Basic singular solutions

By virtue of its linearity, the Laplace equation allows for the constitution of a general solution from combinations of elementary solutions. Some useful solutions are presented in what follows.

Source

A source is a point element from which a flow originates and propagates in all directions equally as shown in Figure 3-2. The potential created by such an element is defined in a spherical coordinate system as:

$$\Phi = -\frac{\sigma}{4\pi r} \tag{3-18}$$

, where σ signifies the source's strength and r is the distance from the point itself. A sink is equivalent to a source by flipping the sign of the strength σ. Computing the gradient of this potential yields the velocity due to this element:

$$\mathbf{u} = \langle u_r, u_\theta, u_\phi \rangle = \langle \frac{\sigma}{4\pi r^2}, 0, 0 \rangle \tag{3-19}$$

A distribution of basic sources can be used to simulate the thickness of an airfoil as per Figure 3-3. However, on its own, a source element does not introduce circulation into the domain and thus does not account for any aerodynamic forces.

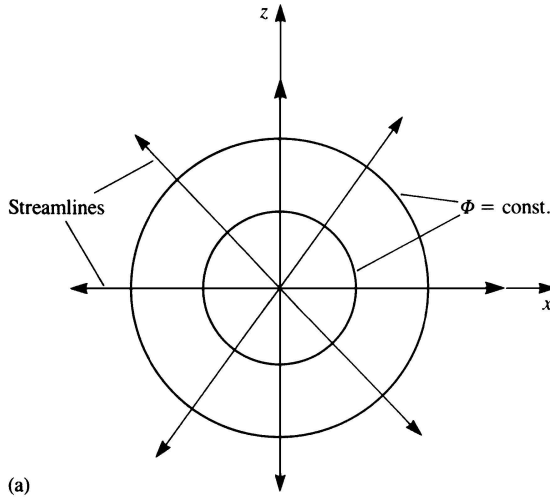

Figure 3-2: Point source, reproduced from [5].

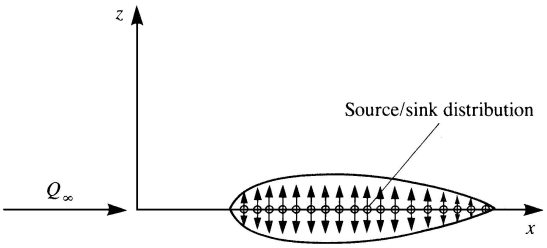

Figure 3-3: Thick airfoil representation by basic source distribution, reproduced from [5].

Doublet

A doublet is another basic solution comprising a combination of a source and a sink situated infinitely close to each other. The potential function can be expressed as:

$$\Phi = \frac{-\boldsymbol{\mu} \cdot \mathbf{r}}{4\pi r^3} \tag{3-20}$$

, where the magnitude of $\boldsymbol{\mu}$ is referred to as the doublet strength and that of $\mathbf{r}$ represents the distance from the doublet core. A doublet has an orientation as defined by the vector $\boldsymbol{\mu}$, as shown in Figure 3-4. The respective induced velocities can be derived as:

$$\mathbf{u} = \langle u_r, u_\theta, u_\phi \rangle = \langle \frac{\mu cos\theta}{2\pi r^3}, \frac{\mu sin\theta}{4\pi r^3}, 0 \rangle \tag{3-21}$$

Doublets are capable of modeling discontinuities, such as those created by thin surfaces, such as flat plates or a wake surface such as S_W on Figure 3-1. These do produce circulation.

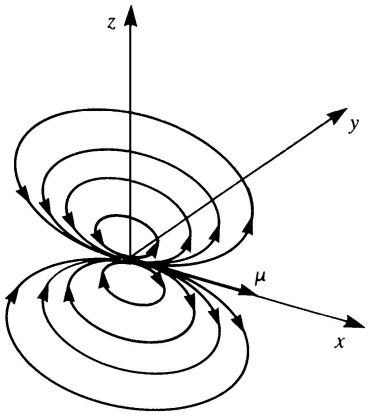

Figure 3-4: Point doublet, reproduced from [5].

Vortex

A point vortex induces circular flow streamlines around it, as shown in Figure 3-5. It is irrotational everywhere except for right at the core, where the vorticity is infinitely large. For the 2D representation, the potential and the velocity are defined as follows, with Γ denoting the strength of the vortex (or the circulation induced by it):

$$\Phi = -\frac{\Gamma}{2\pi}\theta \tag{3-22}$$

$$u_\theta = -\frac{\Gamma}{2\pi r} \tag{3-23}$$

In 3D, the Biot-Savart law can be used to determine the velocity induced by a vortex line. For potential flows, the following principles, referred to as Helmholtz's theorems, apply with regard to vortex filaments:

- The strength of a vortex filament is constant along its length.
- A vortex filament cannot start or end in a fluid; it must extend to infinity or form a closed path.
- In the absence of rotational external forces, a fluid that is initially irrotational remains irrotational.

An extension of these principles is Kelvin's circulation theorem, which stipulates that the circulation around a closed curve consisting of the same fluid elements moving with the fluid remains constant with time. This is expressed in Equation 3-24.

$$\frac{D\Gamma}{Dt} = 0 \tag{3-24}$$

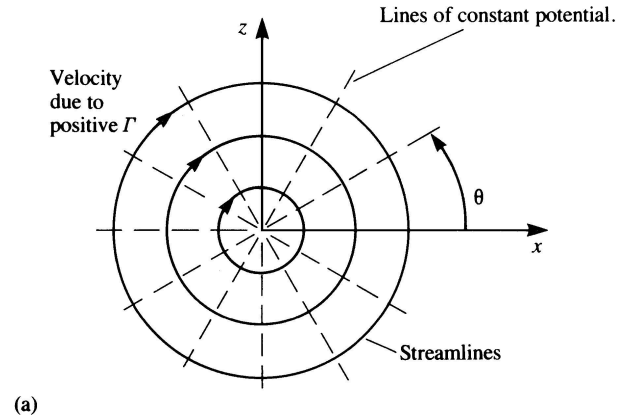

Figure 3-5: Vortex, reproduced from [5].

3-1-3 Boundary condition types

The physical presence of a solid body in the computational domain where the Laplace equation is sought to be solved can be imposed in two ways:

- **Dirichlet BC**. This method entails specifying the value of the potential on the boundary itself. It is also referred to as the "indirect" method to enforce zero normal flow through the solid surface.
- **Neumann BC**. This condition refers directly to specifying zero normal flow through the solid surface.

Considering the boundary S_B shown in Figure 3-6, the following can be stated:

$$-\mu = \Phi - \Phi_i \tag{3-25}$$

$$-\sigma = \frac{\partial \Phi}{\partial n} - \frac{\partial \Phi_i}{\partial n} \tag{3-26}$$

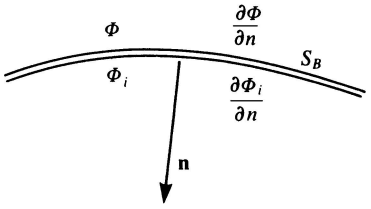

Figure 3-6: Surface boundary S_B, reproduced from [5].

3-1-4 Kutta condition

The Kutta condition relates to the principle that flow must depart smoothly at the trailing edge, irrespective of the edge's finite angle. There are a number of ways in which the Kutta condition can be enforced, as shown in Figure 3-7. This ensures that the circulation around the contour of the body stays finite. This is mathematically expressed through the following relation, where γ denotes the circulation component:

$$\gamma_{TE} = 0 \tag{3-27}$$

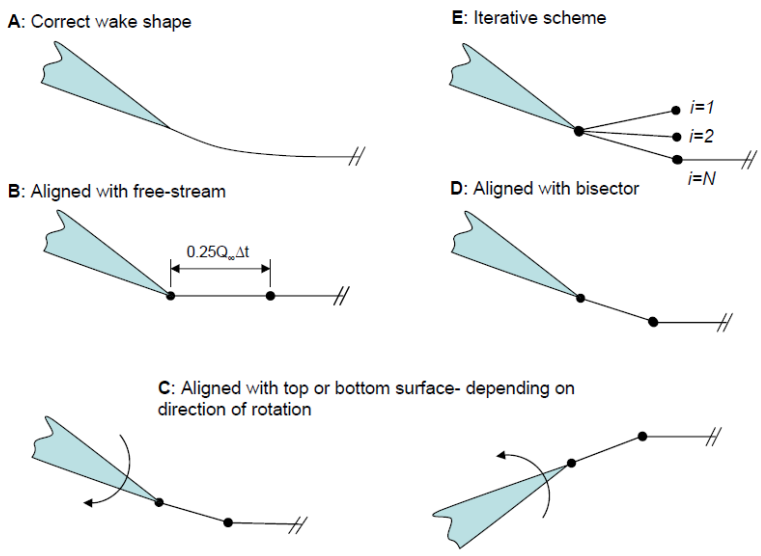

Figure 3-7: Kutta condition formulations, reproduced from [6].

3-2 Lifting line method

Lifting lines employ methods of solving the Laplace equation by representing the body as a series of vortex filaments, jointly forming the lifting line. To compute the flow solution, the following formulation of the Neumann boundary condition is applied:

$$\nabla(\Phi + \Phi_\infty) \cdot \mathbf{n} = 0 \tag{3-28}$$

A typical example is AWSM, an aerodynamic module contained within AeroModule which was developed at the Energy Research Center of the Netherlands (ECN), now merged with the Netherlands Organisation for Applied Scientific Research (TNO). The vorticity bound to the body is represented by a lifting line passing through the quarter-chord location at each cross-section, with vorticity being shed at the trailing edge, where it forms vortex rings. The latter simulates a free wake where the wake itself convects with the local flow velocity. The graphical representation of such a system is shown in Figure 3-8.

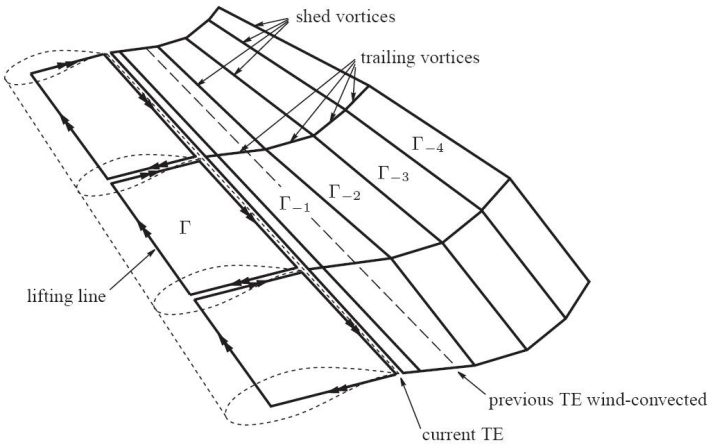

Figure 3-8: AWSM lifting line model geometry, reproduced from [1].

The solution process follows a nonlinear numerical procedure to include the effects of viscosity, which are introduced by specifying the aerodynamic polars of the airfoils representing the cross-section shapes. In this manner, the flow solution is obtained once equilibrium is reached between the strength of the lifting line potential flow elements and strip element forces, as dictated by the section aerodynamic properties. The Kutta-Joukowsky theorem is used to couple the vorticity with the respective aerodynamic force, outlined in Equation 3-29:

$$L' = \rho V \Gamma \tag{3-29}$$

, where L' is the sectional lift, ρ is the fluid density, V is the local flow velocity and Γ is the circulation. At each time step, a new value for the circulation of the bound vortex ring Γ is computed, with the previous one being convected downstream into the wake. The circulation system induces a flow velocity component at the bound vortex location, which modifies the inflow conditions needed to determine the aerodynamic load of the section, which is subsequently related back to the corresponding Γ value prescribed by the Kutta-Joukowsky relationship. This iteration continues until a margin of convergence is met.

The original lifting line theory of Prandtl does not account for sweep that may be applied to a body under consideration [11]. AWSM does make use of a correction factor to model this, namely by means of decomposing the inflow velocity vector into components normal and parallel to the local lifting line and discarding the latter. The solution process subsequently follows its nominal course after applying the decomposition. The motivation behind this approach is rooted in the 2D sweep correction factor known as cross-flow principle, the basics of which are covered later in section 2-1. Additionally, AWSM is capable of correctly representing the local displacement of the bound vortex, as well as the change in orientation caused by the application of sweep.

3-3 Panel method

Panel methods represent a higher fidelity model than lifting line models for inviscid flows by virtue of being able to independently model the thickness and camber of complex 3D shapes without the need to look up sectional aerodynamic data. However, due to the fact that plain panel methods solve for a potential flow, viscosity effects are not modeled, which is a downgrade when compared to lifting line models using sectional aerodynamic data. Additional boundary layer models are required to simulate viscous effects on top of the inviscid solution. On the other hand, an advantage of not having to rely on 2D aerodynamic data is that cross-flow does not have to be neglected, a simplification that is frequently used in lifting line models. Cross-flow is expected to play a larger role in swept geometries, which is why panel methods are expected to give more accurate results in swept regions. The current work sets out to investigate the extent of this effect.

3-3-1 Source doublet method

Reformulating Equation 3-16 for the case where point P is outside of the boundary S_B renders it equal to 0. Combining the two formulations of Equation 3-16 for external and internal potentials Φ and Φ_i, respectively, yields:

$$\Phi(P) = \frac{1}{4\pi}\int_{S_B}\left[\frac{1}{r}\nabla(\Phi-\Phi_i) - (\Phi-\Phi_i)\nabla\frac{1}{r}\right]\cdot\mathbf{n}dS - \frac{1}{4\pi}\int_{S_W}\Phi\mathbf{n}\cdot\nabla\frac{1}{r}dS + \Phi_\infty(P) \tag{3-30}$$

Introducing Equation 3-25 and 3-26 into 3-30 leads to:

$$\Phi(P) = -\frac{1}{4\pi}\int_{S_B}\left[\sigma\left(\frac{1}{r}\right) - \mu\frac{\partial}{\partial n}\left(\frac{1}{r}\right)\right]dS + \frac{1}{4\pi}\int_{S_W}\left[\mu\frac{\partial}{\partial n}\left(\frac{1}{r}\right)\right]dS + \Phi_\infty(P) \tag{3-31}$$

Equation 3-31 represents the governing equation for source doublet methods. Numerical methods must be employed to reach a solution for general cases. The most common boundary condition choice in panel methods is based on the Dirichlet formulation, which prescribes the perturbation potential Φ on S_B. For an enclosed boundary, such as S_B, the zero normal flow through the surface condition dictates that $\partial\Phi_{i,total}/\partial n = 0$, i.e. the velocity potential inside the surface, excluding internal singularities, is constant:

$$\Phi_{i,total} = (\Phi + \Phi_\infty)_i = \text{const} \tag{3-32}$$

The internal velocity potential can thus be set to any constant. A handy choice is to set $\Phi_{i,total} = \Phi_\infty$ in an inertial frame attached to the surface. With these assumptions Equation 3-31 transforms into the following relation:

$$\Phi_i(P) = -\frac{1}{4\pi}\int_{S_B}\left[\sigma\left(\frac{1}{r}\right) - \mu\frac{\partial}{\partial n}\left(\frac{1}{r}\right)\right]dS + \frac{1}{4\pi}\int_{S_W}\left[\mu\frac{\partial}{\partial n}\left(\frac{1}{r}\right)\right]dS = 0 \tag{3-33}$$

Equation 3-33 does not have a unique solution in its current form, as both the source σ and doublet μ terms are unknown. Recalling the Neumann condition and introducing the $\partial\Phi_{i,total}/\partial n = 0$ condition into it leads to:

$$\frac{\partial\Phi}{\partial n} = -\mathbf{n}\cdot\mathbf{Q} \tag{3-34}$$

Given that $\partial\Phi_i/\partial n = 0$ since $\Phi_i = 0$, Equation 3-26 can be rewritten as follows:

$$\sigma = \mathbf{n}\cdot\mathbf{Q} \tag{3-35}$$

, with Q_∞ as the local flow velocity vector. Equation 3-35 predefines the values of the source elements, thus rendering Equation 3-33 to have a unique solution for the doublet strengths μ, provided the unknown μ of the wake is coupled to the μ on S_B, which can be configured using the Kutta condition.

3-3-2 Discretization

In order to solve the potential flow problem formulated earlier, the governing equations and geometry of the problem have to be discretized.

Surface discretization

Panel methods require an adequate representation of the surface describing the solid body since the flow solution in the entire domain depends solely on the solution on the surfaces S_B and S_W. The "panels" themselves, which are a centerpiece of panel methods, refer to the grid elements composing the surface mesh. The usual approach in low order panel method models is to represent the surface by a concatenation of flat quadrilateral elements. This may however lead to gaps in the mesh, especially exacerbated in regions with high curvature and twist, leading to the distortion displayed in Figure 3-9.

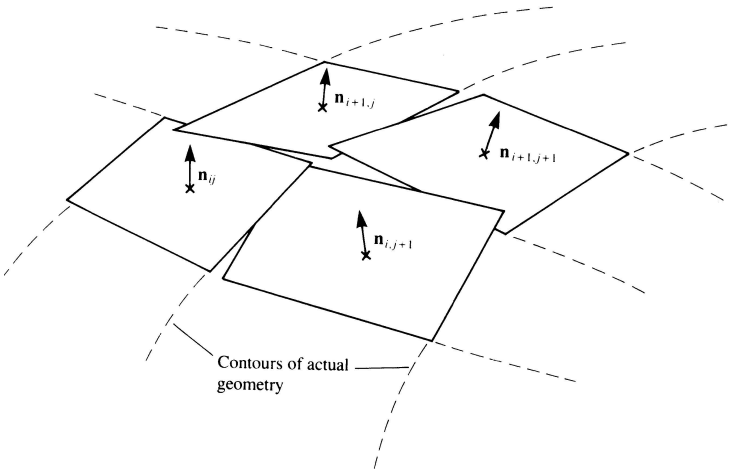

Figure 3-9: Difficulty of representing curved geometry with flat elements, reproduced from [5].

To prevent this inaccuracy, higher order surface discretization may be employed. However, with the computational power available nowadays a sufficient discretization resolution can be imposed to minimize this inaccuracy. A useful approximation of the surface capable of avoiding any gaps is to discretize the surface into rectilinear panels, where the edges are not necessarily coplanar. The edges in this case are straight but do not form flat sides and thus can be curved. Such a mesh element is shown in Figure 3-10.

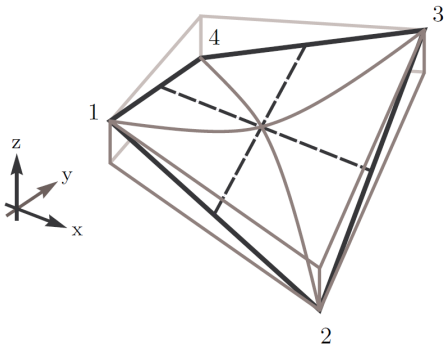

Figure 3-10: Rectilinear panel, reproduced from [7].

At this stage, the collocation points where the boundary conditions on the surface are enforced can be defined. For a Dirichlet approach, Dixon [6] suggests an offset of 1–2% of the respective smallest panel length under the surface S_B, applied in the middle of the panel to avoid numerical errors. Such an arrangement is visualized in a 2D perspective in Figure 3-11.

Singularity element discretization

The discretized geometry also serves as a support for the surface singularity elements describing the source and doublet contributions. Such a distribution of surface elements is presented in Figure 3-12. Similar to the geometric surface discretization, the strength of these singularity elements can be approximated by piecewise polynomials of various orders. Elementary 3D panel method models make use of 0-order 3D singularity distributions where each source and doublet strength are assigned a constant value over the entire surface of each panel.

The wake panels are modeled by doublet elements, the strength of which is determined by the Kutta condition at the time when these are shed from the body at the emission line. The surface of the

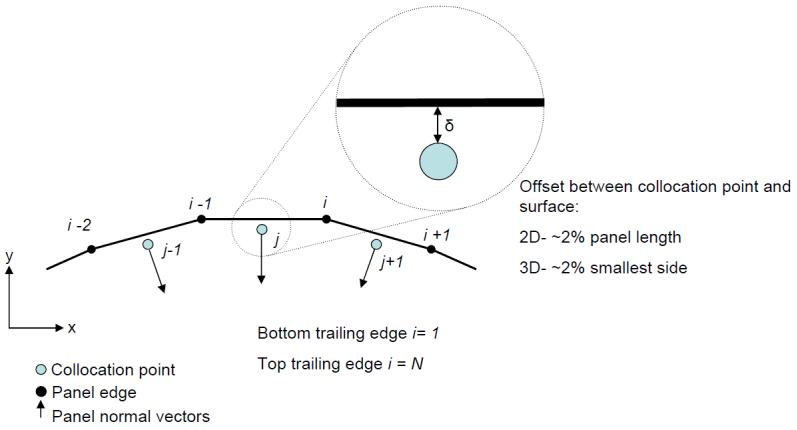

Figure 3-11: Collocation point definition in 2D, reproduced from [6].

wake is not solid, thus the non-entry boundary conditions do not extend here. For a free wake model, the wake surfaces convect with the local flow velocity, which includes a contribution from the entire induction system. This leads to wake deformation in the form of wake roll-up.

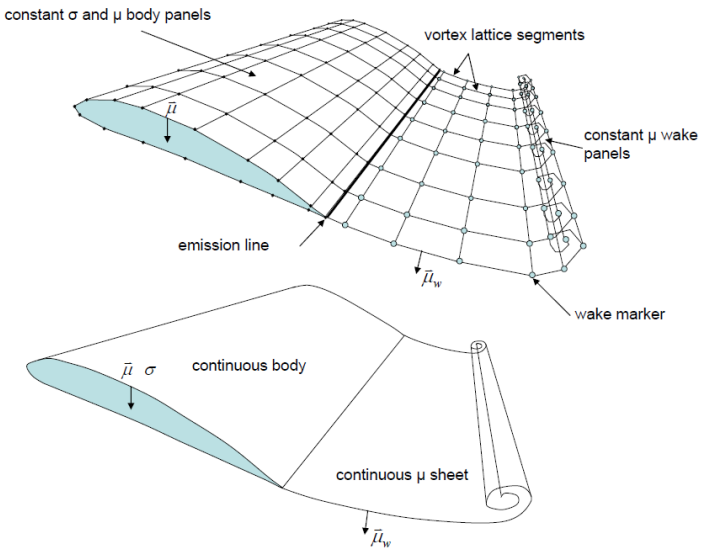

Figure 3-12: Panel method geometry, reproduced from [6].

An optimal use of computing resources may be achieved by locally increasing the modeling accuracy in specific regions of interest. This is done by increasing the discretization resolution where it matters, such as in locations with large gradients of flow properties or geometry, regions prone to numerical instabilities or discontinuities. Typical examples of such regions are the leading and trailing edges and the blade tip. To this end, a useful distribution of points around the cross-section that may be used is given by a cosine spacing rule, shown in Figure 3-13 and expressed by:

$$x = \frac{c}{2}(1 - \cos\beta) \tag{3-36}$$

, where β is the angular coordinate on Figure 3-13, c is the chord length and x is the resulting grid point coordinate along the chord line.

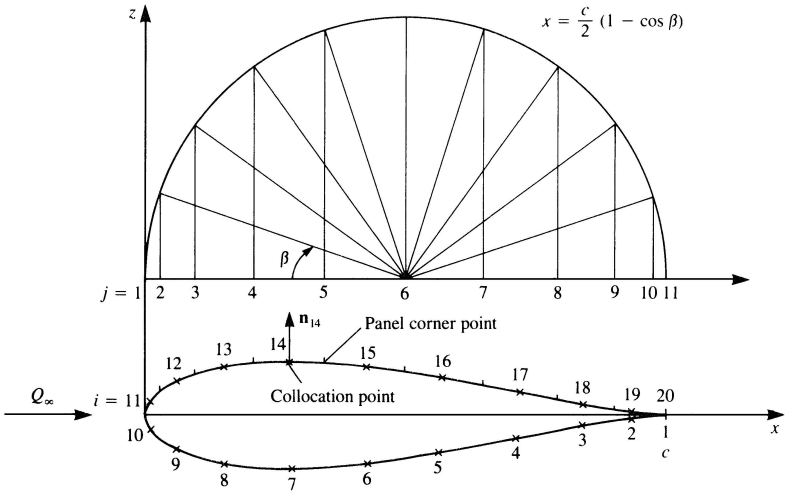

Figure 3-13: Cosine spacing rule, reproduced from [5].

A similar rule can be derived in the spanwise direction to ensure appropriate resolution at the blade tip.

Boundary condition discretization

For the case where the internal potential Φ_i^* is set equal to Φ_∞, the source strength is predefined as per Equation 3-35. The governing equation outlined in Equation 3-37 is enforced at each collocation point, with the sums adding up the contributions of all the singularity elements present on the body and the wake.

$$\sum_{j=1}^{N_{bodypanels}} \frac{-1}{4\pi} \int_{S_{Body,j}} \mu_j \frac{\partial}{\partial n_j}\left(\frac{1}{r_{ij}}\right) dS_j + \sum_{j=1}^{N_{bodypanels}} \int_{S_{Body,j}} \sigma_j \frac{1}{r_{ij}} dS_j + \sum_{k=1}^{N_{wakepanels}} \frac{-1}{4\pi} \int_{S_{wake,k}} \mu_k \frac{\partial}{\partial n_k}\left(\frac{1}{r_{ij}}\right) dS_k = 0 \tag{3-37}$$

, which can be solved using the following relations that form a linear system of equations:

$$A_{ij} = \frac{-1}{4\pi} \int_{S_j} \frac{\partial}{\partial n_j}\left(\frac{1}{r_{ij}}\right) dS_j \tag{3-38}$$

$$B_{ij} = \int_{S_j} \frac{1}{r_{ij}} dS_j \tag{3-39}$$

$$C_{ik} = \frac{1}{4\pi} \int_{S_k} \frac{\partial}{\partial n_k}\left(\frac{1}{r_{ik}}\right) dS_k \tag{3-40}$$

$$A_{ij}\mu_j + B_{ij}\sigma_j + C_{ik}\mu_k = 0 \tag{3-41}$$

$$i, j = 1..N_{\text{body panels}} \tag{3-42}$$

$$k = 1..N_{\text{wake panels}} \tag{3-43}$$

The influence coefficients composing the A_{ij}, B_{ij} and C_{ik} matrices have been evaluated for flat constant-strength quadrilateral sources and doublets by Hess and Smith [29]. To apply these directly, special treatment is required to "flatten" the curved quadrilateral surface elements. A common approach is to declare an average plane defined by the diagonals of the quadrilateral. The corners of the panel elements can then be projected onto the average plane and thereafter form flat surfaces suited for the evaluation of elementary influence coefficients. A similar approach entails splitting the quadrilateral into triangular surfaces sharing one of the quadrilateral's diagonals. For practicality, the flat triangular surface solutions may be recombined to represent the quadrilateral ensemble they form. The triangular formulation is a better approximation of the curved surface, however it may be more computationally expensive. Ultimately, the two methods should converge with sufficient discretization resolution. A refined approach of evaluating the doublet contribution is used by van Garrel [7]. The influence coefficient of a doublet represents the solid angle formed by its projection on a sphere with a unit radius centered at the evaluation point. A schematic is provided in Figure 3-14. The solid angle is then equal to the ratio of the areas of the projection and that of the sphere.

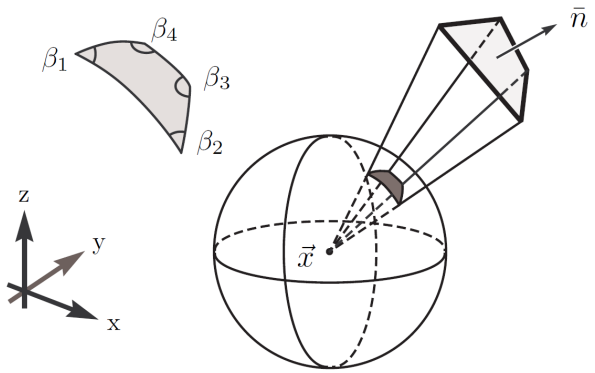

Figure 3-14: Doublet and vortex ring equivalence, reproduced from [7].

The only unknown left in Equation 3-41 is the μ_j distribution. The values of σ_j are predefined in Equation 3-35, while μ_k is known a priori from previous steps. The most recent wake panel strength however must be computed too and it follows from the Kutta condition through Equation 3-44.

$$\mu_{\text{wake, attached}} = \mu_{\text{TE, top}} - \mu_{\text{TE, bottom}} \tag{3-44}$$

To alleviate some of the computational expenses associated to the computation of the C_{ik} matrix for an expanded wake, the approach adopted by Bernardini is used [8, 30]. The surface of the wake is subdivided into a doublet wake in the vicinity of the body and a vortex wake further downstream, as shown in Figure 3-15. Bernardini refers to the doublet wake as one of the components of the scattered potential along with the body-attached doublet and source potential, getting the full treatment of Equation 3-40. The vortex wake in turn contributes to the so-called incident potential, the influence of which is taken into account via the velocity it induces at the evaluation points, as evaluated by the Biot-Savart law. To incorporate it into the governing boundary condition described by Equation 3-37, this velocity is added up to the free stream velocity component used in the predefinition of the bound source term strengths following Equation 3-35, resulting in Equation 3-45. The author does not prescribe a cut-off distance to delimit between the doublet and vortex wakes. This shall be tailored per application. Placing the cut-off one chord length away from the trailing edge yielded has been shown to cause $< 1\%$ error in tests of quasi-2D flows.

$$\sigma = \mathbf{n} \cdot (\mathbf{Q}_\infty + \mathbf{\Omega} \times \mathbf{r} + \mathbf{u}_{\text{vortex wake}}) \tag{3-45}$$

, where $\mathbf{Q}_\infty$ is the onset flow velocity, $\mathbf{\Omega}$ is an angular velocity applied to the body, $\mathbf{r}$ is the position vector from the rotation center to the panel collocation point, and $\mathbf{u}_{\text{vortex wake}}$ is the vortex wake induced velocity at the collocation point.

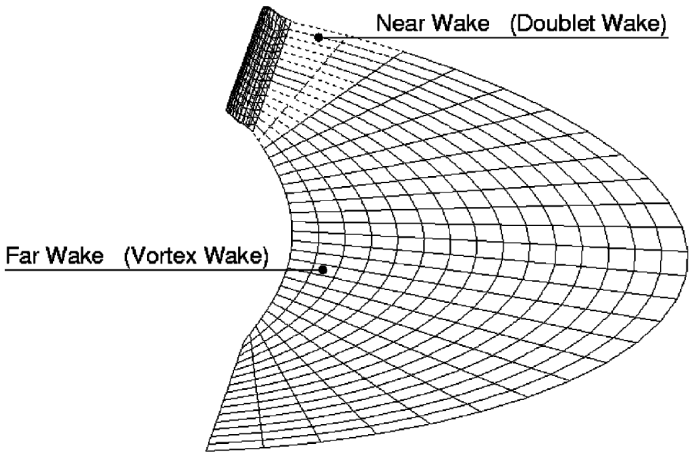

Figure 3-15: Separation of wake into doublet and vortex wake, reproduced from [8].

The equivalence of a quadrilateral doublet element with a vortex ring, where the surface doublet strength is equated with the vortex filament strength, as shown in Figure 3-16, can be exploited. The velocity induced by a curved doublet panel can be computed by treating it as a twisted vortex ring defined by its contour.

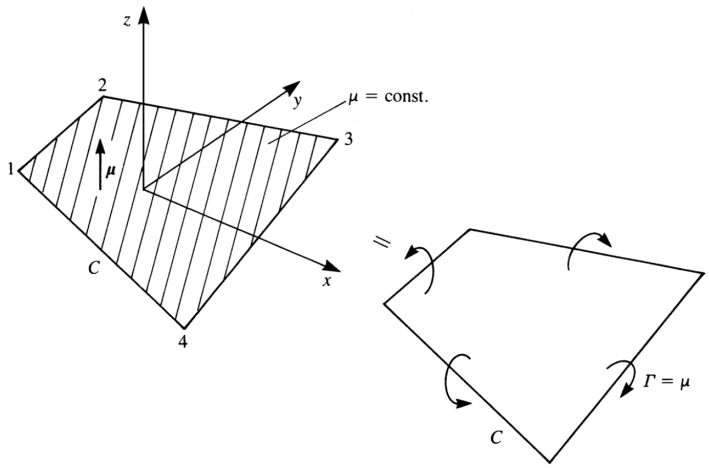

Figure 3-16: Doublet and vortex ring equivalence, reproduced from [5].

Surface velocity

To determine the aerodynamic loads exerted on the body, the velocity tangential to the surface must be computed first. A method frequently employed in panel methods to that end is the one introduced by Maskew [31] in the VSAERO panel code.

$$\vec{u}_S = -\nabla_S \mu \tag{3-46}$$

Equation 3-46 is known to give good results, although no formal proof to support its validity is provided. An alternative approach to determine the surface perturbation velocity based on a mathematical derivation is proposed by Marcov [32, 268-271]:

$$\vec{u}_S = -\frac{1}{2}\nabla_S \mu + \vec{w} \tag{3-47}$$

, where $\vec{w}$ stands for the Cauchy principal value of the potential gradient contribution of the boundary. Baayen [9] ran tests to quantify the difference that the two methods for obtaining the surface velocity produce in terms of the flow solution for a simple NACA0012 wing. Vortexje, the code developed by Baayen, implements the method elaborated by Marcov. The results of Vortexje are then compared with the results of XFLR5, which bases its surface velocity computation on the method outlined in VSAERO. The results are plotted in Figure 3-17.

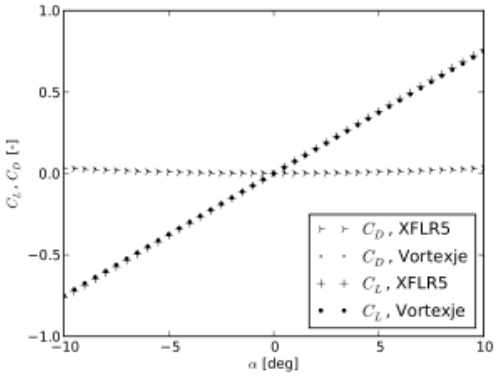

Figure 3-17: Comparison between XFLR5 and Vortexje, reproduced from [9].

Both these methods require the evaluation of the derivative of the velocity potential. Numerical differentiation based on finite differences may be used to approximate the derivative. Starting from the obtained discrete distribution of μ at the collocation points, neighboring panels can be connected to compute the derivative along the connecting line. Such a method is used by Dixon [6], where values of the two adjacent panels along a dimension are used to fit the doublet strengths to a quadratic curve. The grid representation for this process is shown in Figure 3-18.

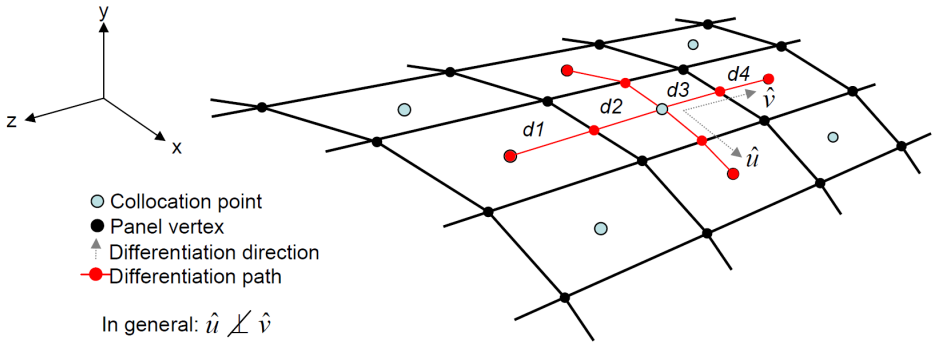

Figure 3-18: Surface velocity differentiation grid, reproduced from [6].

The contribution of the derivatives along each direction $\hat{d}_j$ can be summed to create a weighted average, as per Equation 3-48:

$$u_i = \frac{\sum_{j=1}^{n} \frac{\partial \mu}{\partial d_j} \hat{d}_j \cdot \hat{u}_i}{\sum_{j=1}^{n} \hat{d}_j \cdot \hat{u}_i} \tag{3-48}$$

Another approach to estimating $\nabla_S \mu$ on the 3D surface makes use of the divergence theorem, as implemented by van Garrel [10]. The surface region where the divergence theorem is applied is presented in Figure 3-19.

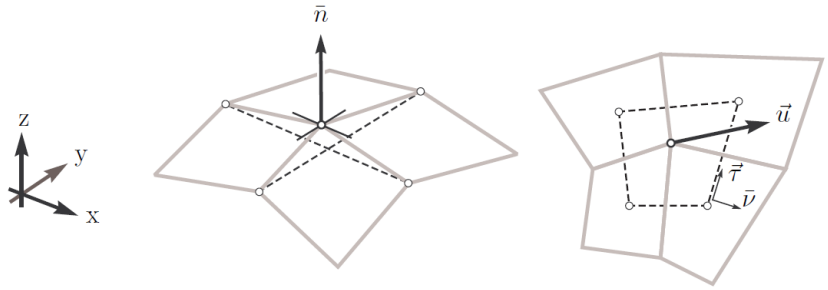

Figure 3-19: Contour velocity interpolation, reproduced from [10].

The surface S with boundary ∂S is defined by the lines connecting the collocation points of 4 adjacent panels. A normal vector $\vec{n}$ is determined from the 4 end-points of the intersection lines of the panels. Subsequently, this average normal vector and $\vec{\tau}$, the vector tangential to the boundary, are used to define the $\vec{v}$ vector which is outward normal to the contour and tangential to the surface S.

$$\iint_S \nabla_S \mu \, dS = \int_{\partial S} \mu \vec{v} \, dl \tag{3-49}$$

$$\vec{v} = \frac{\vec{\tau} \times \vec{n}}{|\vec{\tau} \times \vec{n}|} \tag{3-50}$$

The perturbation velocity at the grid point connecting the 4 panels is assigned the average potential gradient of surface S as computed by Equation 3-51.

$$\overline{\nabla_S \mu} = \frac{1}{S} \int_{\partial S} \mu \vec{v} \, dl \tag{3-51}$$

Pressure discretization

Having determined the perturbation velocity, Equation 3-9 which determines the pressure coefficient can be rewritten to account for the applied panel discretization, as per Equation 3-52:

$$c_p = 1 - \frac{u^2}{u_{ref}^2} - \frac{2}{u_{ref}^2} \frac{\partial \Phi}{\partial t} = 1 - \frac{\left(\vec{\tau} \cdot \left(\vec{Q}_\infty + \vec{\Omega} \times \vec{r}\right) + u_S\right)^2}{u_{ref}^2} + \frac{2}{u_{ref}^2} \frac{\mu_t - \mu_{t-1}}{\Delta t} \tag{3-52}$$

, where $\vec{\tau}$ denotes a vector tangential to the panel surface used to project the kinematic velocity onto the panel, $\vec{\Omega}$ is an angular velocity applied to the body, $\vec{r}$ is the position vector from the rotation center to the panel collocation point, μ_t and μ_{t-1} refer to the panel doublet strength at time t and $t-1$, respectively, and Δt is the time step used for the simple first-order Eulerian time marching scheme. $\vec{u}_{ref}$ is then commonly defined in panel codes as:

$$\vec{u}_{ref} = \vec{Q}_\infty + \vec{\Omega} \times \vec{r} \tag{3-53}$$

Equation 3-53 presumes that the reference velocity used in the definition of the c_p may vary per panel pertaining to the same cross-sectional slice even for a uniform flow $\vec{Q}_\infty$, as the position vector r may vary. Lastly, by integrating the pressure distribution over the surface, the forces and moments can be obtained. In the discretized case, Equation 3-54 applies.

$$\Delta\vec{F} = -c_p \frac{1}{2}\rho u_{ref}^2 \Delta S \vec{n} \tag{3-54}$$

3-4 AWSM3D Summary of implementation

The panel code created in this study is named AWSM3D, as an extension of AeroModule's AWSM model. A breakdown of its implementation strategies and algorithms is presented in Table 3-1.

Table 3-1: AWSM3D implementation summary (initial commit).

Meshing		
Grid structure	1.1	Rectangular grid of panels structured into a #chordwise by #spanwise matrix.
	1.2	Chordwise index starts at LE and goes around the strip starting through the upper surface.
	1.3	The mesh file is supplied in MSH format version 2 (*version-number*=2.2) [33, 34], following above-mentioned nomenclature.
Mesh element type	1.4	Quadrilaterals (default) flattened by projection onto average plane.
	1.5	Triangular panels (implemented), which later recombine into quadrilaterals.
Tip treatment	1.6	Cut-off (recommended) – open gap at extremity.
	1.7	Triangular sharp tip patches expressed as quadrilaterals with one zero length side (implemented). Coarse approximations used.
Spacing	1.8	Cosine spacing recommended in spanwise and chordwise directions. Special care to avoid numerical instability at TE due to close proximity of collocation points.
Singularity elements		
Boundary conditions	2.1	Dirichlet (default).
	2.2	Neumann (implemented). Method susceptible to error in the vicinity of the TE.
Bound circulation	2.3	Flat source and doublet solutions by Hess and Smith [29].
	2.4	For Neumann formulation, doublets surfaces equated to vortex rings.
Wake circulation	2.5	Split into doublet and vortex wake, according to Bernardini [8].
	2.6	Latest $n = 4$ panels of wake treated as doublets whose velocity potential is considered following method of Equation 3-40. Parameter n is customizable. Wake doublet panels quadrilaterals are flattened (default), therefore special care if choice of n extends to highly-deformed wake downstream – consider triangular formulation.
	2.7	Rest of the wake treated as vortex rings whose velocity potential is expressed via their contribution to the bound source term strength as per Equation 3-35.
	2.8	Attached vortex ring aligned with free stream (see Figure 3-7).
Kutta condition	2.9	Velocity potential at TE formulation (see Equation 3-29).
Collocation points	2.10	Located at a depth of 2% of the corresponding smallest panel length into the body.
Circulation system post-processing		
Surface velocity	3.1	Second-order central finite difference scheme deriving from [31].
Pressure computation	3.2	Bernouilli per (see Equation 3-52).
	3.3	Unsteady formulation not yet validated.
Load computation	3.4	Pressure integrated over chordwise strips.

Chapter 4

Panel method validation cases

Chapter 4 details a number of geometries for which exact solutions have been derived. These will be used to validate the panel method model under development. The validation cases initially involve elementary 2D shapes and later on gradually build up in complexity, eventually reaching the final desired level of complex 3D bodies. To properly resolve the latter, a few established panel codes are presented, along with lower fidelity or 2D aerodynamic solvers.

4-1 Established aerodynamic solvers

A few established aerodynamic models are introduced. These are used throughout this chapter for the validation of the panel code under development for the cases considered, where appropriate.

2D solvers

XFOIL is a high-order 2D panel method written by Dr. Mark Drela at MIT [35]. Its accuracy and robustness have established it as a reliable and widely adopted resource in the field of aerodynamics. The airfoil surface is discretized with vortex sheets with a linearly varying strength and source sheets of constant strength. It is capable of solving viscous flows by employing boundary layer models. However, for the purposes of this work, only the inviscid mode in which the wake vanishes is considered.

JavaFoil is a similar 2D panel method code, written by Martin Hepperle [36]. It employs the same method as XFOIL, and therefore has the same level of accuracy. The advantage it has over XFOIL is the modern user interface and the presence of a database of common airfoils, some of which are known to be analytically solvable, and post-processing capabilities to remove data noise when plotting solutions within the software itself.

3D solvers

XFLR5 is an aerodynamic analysis tool comprising a wrapper for XFOIL, a lifting line model, a vortex lattice model, and a 3D panel model based on elementary source-doublet panel method. Unsteady flows fall outside the scope of its capabilities. Due to its rigid integration of the solver with its graphical user interface specifically designed for fixed flight, it is cumbersome to apply the model to

aerodynamic bodies that do not fall into the category of fixed wing aircraft. Modifying the source code to allow for some flexibility, such as including unsteady effects or being able to import custom geometries or flow setups, was deemed impractical and inefficient up to the point that it led to the creation of alternative panel method codes from scratch, as in the case of Vortexje.

Vortexje is an open-source 3D panel code written in C++ developed to allow more freedom than XFLR5 [9]. More importantly, it allows for custom geometry importing and more complex flow cases, partly by means of granting users better access to its source code. It is based on an elementary source-doublet panel method formulation using constant strength elements. Its primary aim is dynamical system simulation, suitably geared for resolving flows around kites, as a prime example. Its main functional difference from XFLR5 in determining the steady flow solution lies in the surface velocity determination method, as shown in section 3-3-2.

The AeroModule package contains the AWSM lifting line, whose functioning principles are detailed in section 3-2, and a BEM model. As the panel code under development is intended as an extension of AeroModule itself, many algorithms and auxiliary methods will be shared among the three. For that reason, this comparison will likely exclude any secondary sources of discrepancies and shall serve as the closest conceptual comparison between the respective model types.

General panel codes are capable of analyzing more complex shapes as these are not limited to elementary shapes in the same way that analytical solutions are. The associated risk, therefore, comes from the lack of a theoretical backbone to prove a numerical solution of a panel code for a general case. Nonetheless, this is a test to verify whether the developed panel code is on par with established panel codes.

4-2 2D circular cylinder

An analytical potential flow solution exists for an elementary circular cylinder. It results from the superposition of a doublet and a uniform flow term, as shown in Figure 4-1. The mild gradients of the resulting flow and geometry render this flow case as one of the easiest thick geometries that a panel method code can solve.

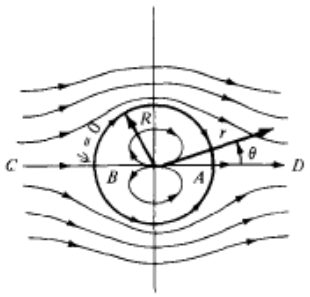

Figure 4-1: Flow around cylinder, reproduced from [11].

In [11] the following velocities are derived for a circular cylinder submerged in uniform flow:

$$u_r = \left(1 - \frac{R^2}{r^2}\right) U_\infty cos\theta \tag{4-1}$$

$$u_\theta = -\left(1 + \frac{R^2}{r^2}\right) U_\infty sin\theta \tag{4-2}$$

, where u_r and u_θ are the polar velocity components, R is the radius of the cylinder, r is the position vector, U_∞ is the inflow velocity, and θ is the angular coordinate.

In order to simulate a 2D flow case with the 3D panel code, a quasi-2D flow is devised by employing a very large aspect ratio circular cylinder (AR=300). By examining the mid-section of this cylinder, the influence of the trailing vortices in the wake vanishes, and therefore the flow regime is virtually 2D. The resulting tangential velocity and pressure coefficient distributions around the cylinder are shown in Figure 4-2 for the developed code, the theoretical solution, the XFOIL curve, and the panel model mode of XFLR5 (denoted by XFLR5 3D). The more challenging flow region to predict for the panel codes, and XFOIL to a lesser extent, were the two peaks at $\pm\pi/2$.

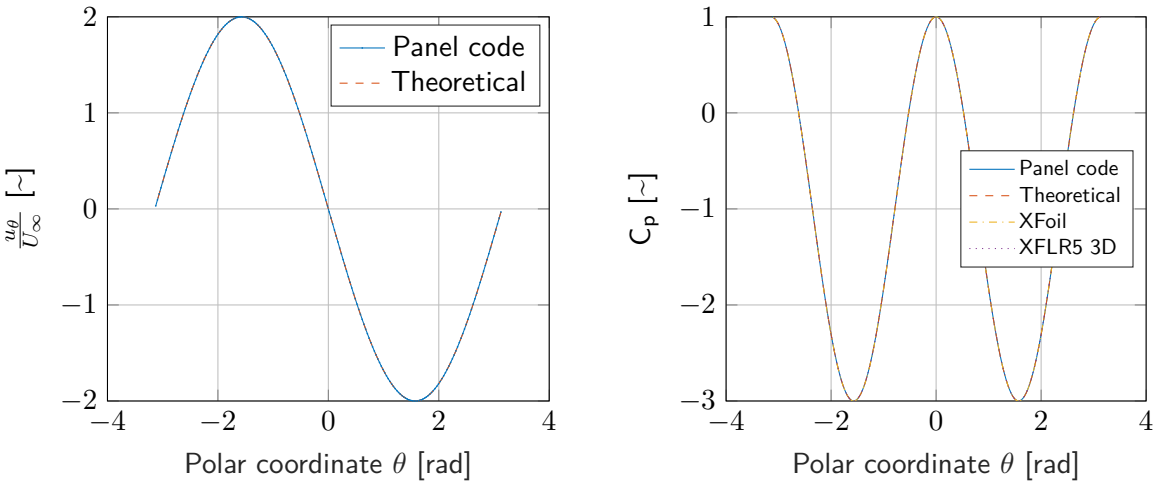

Figure 4-2: Non-dimensionalized tangential velocity (a) and pressure coefficient (b) of quasi-2D flow over cylinder discretized using 200 panels.

4-3 2D van de Vooren airfoil

The van de Vooren airfoil is a particular profile that allows for an analytical solution using the method of conformal mapping. In the context of developing a panel code, the van de Vooren airfoil serves as a good starting point for panel code validation for airfoils with sharp trailing edges, allowing for a more natural implementation of the Kutta condition in comparison with the 2D cylinder case. Additionally, it offers a much stabler numerical problem than the notoriously difficult to solve by panel method Joukowski airfoil, whose cusped trailing edge region requires special attention.

The main parameters of a van de Vooren airfoil are ϵ, which models the thickness, k, which describes the finite trailing edge angle, and l, which dictates the chord length. It is noteworthy that not every trailing edge angle and thickness combination is compatible. As no explicit relation between the two has been derived, the method of creating such a shape is iterative. The k and l parameters are marked on Figure 4-3.

The analytical solution for the Van de Vooren airfoil is taken from [5]. The chord length is equal to $2l$ and relates to other section parameters as:

$$2l = \frac{a2^k}{(1+\epsilon)^{k-1}} \tag{4-3}$$

, where a is the radius of the circle $f = ae^{i\theta}$ in the conformal mapping plane shown on the left graph of Figure 4-3.

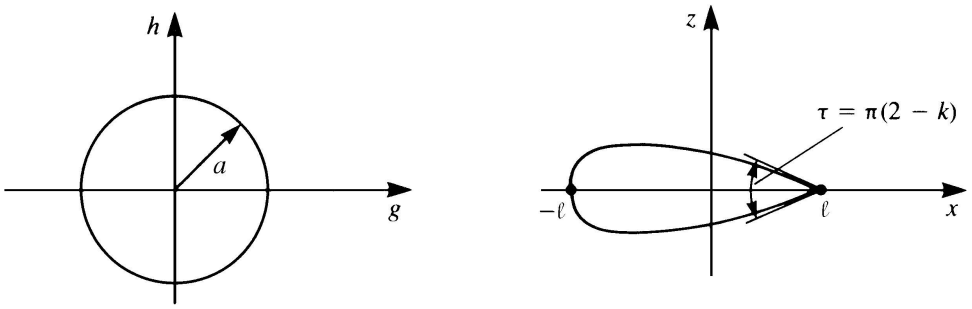

Figure 4-3: Van de Vooren airfoil conformal mapping, reproduced from [5].

$$x = \frac{r_1^k}{r_2^{k-1}} \left[\cos k\theta_1 \cos\left(k-1\right)\theta_2 + \sin k\theta_1 \sin\left(k-1\right)\theta_2\right] \tag{4-4}$$

$$z = \frac{r_1^k}{r_2^{k-1}} \left[\sin k\theta_1 \cos\left(k-1\right)\theta_2 - \cos k\theta_1 \sin\left(k-1\right)\theta_2\right] \tag{4-5}$$

, which makes use of the following parameters:

$$r_1 = \sqrt{\left(a\cos\theta - a\right)^2 + a^2\sin^2\theta} \tag{4-6}$$

$$r_2 = \sqrt{\left(a\cos\theta - \epsilon a\right)^2 + a^2\sin^2\theta} \tag{4-7}$$

$$\theta_1 = \tan^{-1}\frac{a\sin\theta}{a\cos\theta - a} + \pi \tag{4-8}$$

$$\theta_2 = \tan^{-1}\frac{a\sin\theta}{a\cos\theta - \epsilon a} + n_1\pi \tag{4-9}$$

θ here represents the polar angle on the f circle. In Equation 4-9 the n_1 parameter changes based on the quadrant where θ_2 is calculated, being equal to 0 in the first quadrant, 1 in the second and third quadrants and 2 in the fourth quadrant. The velocities along x and z correspondingly then follow from:

$$u = 2Q_\infty \frac{r_2^k}{r_1^{k-1}} \frac{\sin\alpha - \sin\left(\alpha-\theta\right)}{D_1^2 + D_2^2} \left(D_1\sin\theta + D_2\cos\theta\right) \tag{4-10}$$

$$w = -2Q_\infty \frac{r_2^k}{r_1^{k-1}} \frac{\sin\alpha - \sin\left(\alpha-\theta\right)}{D_1^2 + D_2^2} \left(D_1\cos\theta + D_2\sin\theta\right) \tag{4-11}$$

, which make use of the following parameters:

$$A = \cos\left(k-1\right)\theta_1 \cos k\theta_2 + \sin\left(k-1\right)\theta_1 \sin k\theta_2 \tag{4-12}$$

$$B = \sin\left(k-1\right)\theta_1 \cos k\theta_2 - \cos\left(k-1\right)\theta_1 \sin k\theta_2 \tag{4-13}$$

$$D_0 = a\left(1 - k + k\epsilon\right) \tag{4-14}$$

$$D_1 = A\left(a\cos\theta - D_0\right) - Ba\sin\theta \tag{4-15}$$

$$D_2 = A\left(a\sin\theta\right) + B\left(a\cos\theta - D_0\right) \tag{4-16}$$

The Van de Vooren airfoil parameters are selected such that a $t/c = 0.24$ and a TE angle $= 30°$ airfoil is generated. The resulting shape is shown in Figure 4-4. This set of characteristics with mild gradients should impose no additional numerical challenges for the panel code.

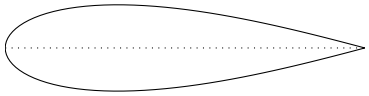

Figure 4-4: Van de Vooren airfoil with $t/c = 0.24$ and TE angle $= 30°$.

The panel code under development and the one in XFLR5 use a 3D geometry with high aspect ratio of 250 to simulate a quasi-2D flow at the midsection. The mesh is discretized using 200 cosine-spaced panels chordwise and 50 panels spanwise. The respective results are plotted in Figure 4-5 against the analytical and JavaFoil results for $\alpha = 5°$, for which the non-zero circulation results in shedding a wake. The 3D panel codes show very good agreement with the other solutions. Minor deviations are found at the location of the suction side peak and towards the trailing edge. The panel code shows signs of an undershoot at the peak, whereas the trailing edge region is better resolved. The XFLR5 3D overshoots the peak but also fares worse around the trailing edge.

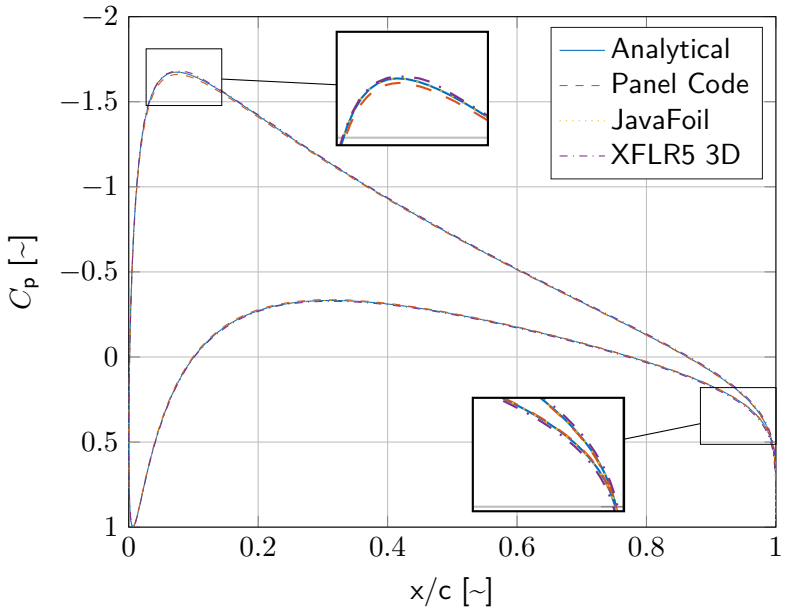

Figure 4-5: Pressure coefficient chordwise distribution for quasi-2D flow around van de Vooren airfoil discretized using 200 panels with AR $= 250$ in axial flow at $\alpha = 5°$.

The same flow case was rerun for a range of angles of attack, the ensuing results being plotted in Figure 4-6. The lift coefficient in this case was obtained via integration of the pressure distribution,

although computing it via the Kutta-Joukowski theorem also yields very similar results. As expected, due to the virtual absence of a wake, the resulting polar is linear. The XFOIL curve follows the analytical solution very well, whereas the panel code results show a progressive undershoot for larger angles of attack.

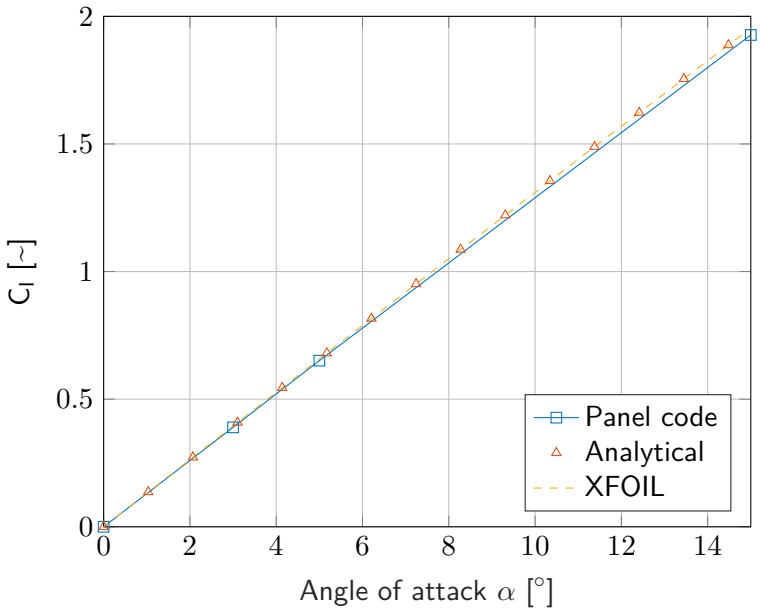

Figure 4-6: Lift coefficient curve for quasi-2D flow around van de Vooren airfoil discretized using 200 panels with AR = 250 in axial flow.

A sensitivity analysis was conducted to investigate the influence of the mesh resolution and collocation point depth expressed as a fraction of the smallest corresponding mesh element length. First, as per Figure 4-7a, a finer discretized mesh produced more accurate results, especially in the vicinity of problematic areas such as the suction side peak, although the difference between the 200 and 300 panel resolutions is indiscernible. Inspecting Figure 4-7b, it becomes apparent that collocation point depth variation in the range of 0.5% – 2% is inconsequential for the determination of aerodynamic loading.

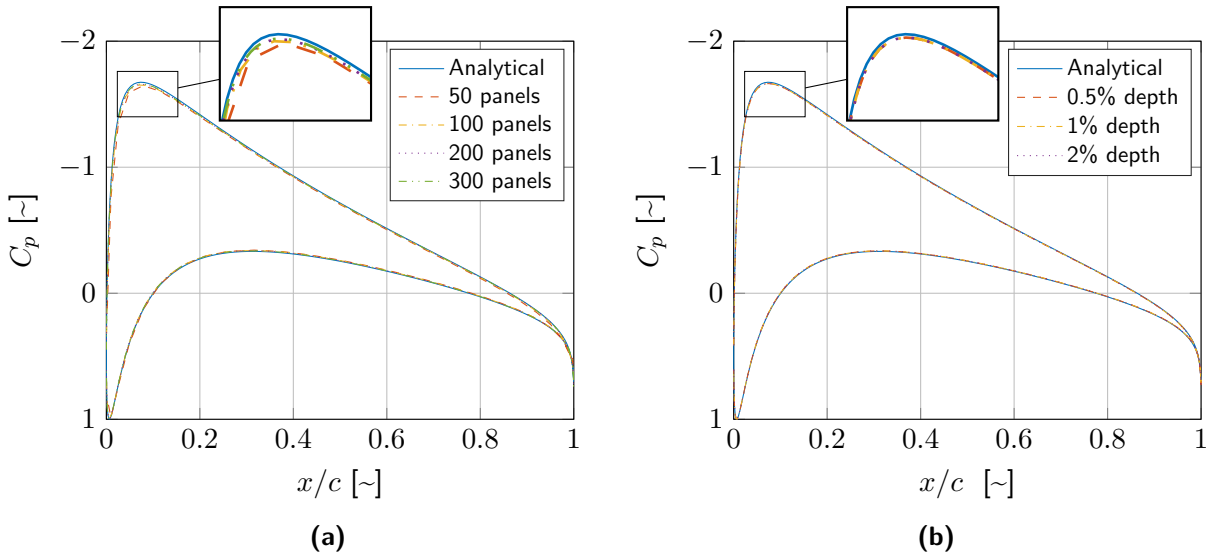

Figure 4-7: Sensitivity of pressure coefficient results to mesh resolution (a) and collocation point depth expressed as a fraction of the smallest corresponding mesh element length (b) of quasi-2D flow around van de Vooren airfoil discretized using 200 panels with AR $= 250$ in axial flow at $\alpha = 5°$.

4-4 3D unit sphere

Similar to the cylinder case in 2D, the 3D sphere represents one of the easiest 3D bodies to be analyzed by means of a panel code. Due to no circulation being produced, there is no wake attached in this case. Again, a uniform flow is superimposed over a 3D doublet to model a spherical body. In [11] the following equations for the potential, polar velocities, and pressure coefficients have been derived:

$$\Phi = U_\infty \cos\theta \left(r + \frac{R^3}{2r^2} \right) \tag{4-17}$$

$$u_r = U_\infty \cos\theta \left(1 - \frac{R^3}{r^3} \right) \tag{4-18}$$

$$u_\theta = -U_\infty \sin\theta \left(1 + \frac{R^3}{2r^3} \right) \tag{4-19}$$

$$c_p = 1 - \frac{9}{4} \sin^2\theta \tag{4-20}$$

The respective coordinates used in these equations are in accordance to Figure 4-8.

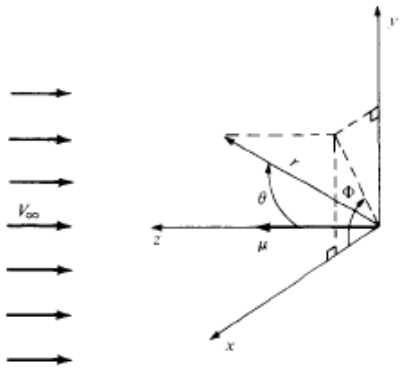

Figure 4-8: Sphere coordinates, reproduced from [11].

The panel code results for the sphere case are shown in Figure 4-9 for a mesh using 100x99 panels. The peaks at $\pm\pi/2$ are captured well. The expected flow symmetry can be observed by rotating the dotted section around the axis attached to the incoming flow vector.

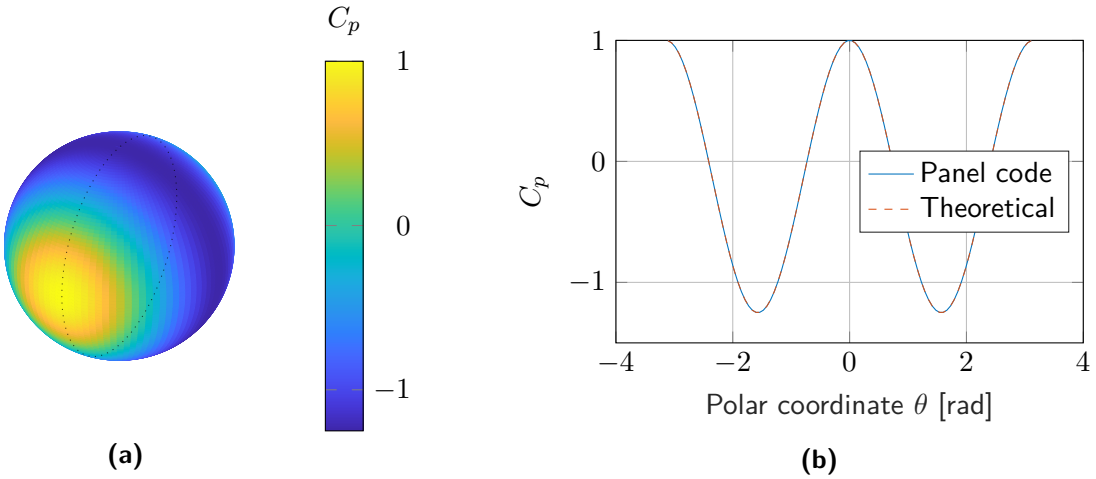

Figure 4-9: Pressure coefficient over sphere surface (a) and around the dotted section (b) immersed in uniform flow using 100x99 panels.

4-5 3D elliptical wing

An analytical solution exists for an elliptical planform formed by a flat plate. From theory it can be derived that for an elliptical chord distribution, such a wing would exhibit the same constant value of downwash at all spanwise locations, creating an elliptical distribution of circulation spanwise, as sketched in Figure 4-10:

$$\Gamma(y) = \Gamma_0 \sqrt{1 - \left(\frac{2y}{b}\right)^2} \tag{4-21}$$

, where y represents the coordinate along the wingspan, Γ_0 is the circulation at the midspan, and b is the wingspan.

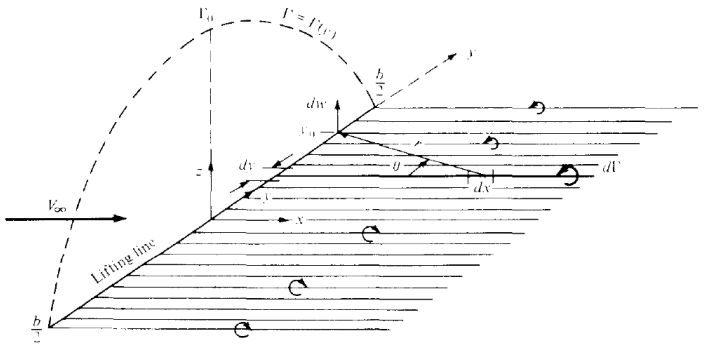

Figure 4-10: Elliptical circulation distribution, reproduced from [11].

As such, this is the first finite wing validation case with a clear discontinuity, as opposed to the first 3D body case tested, the unit sphere, which had a continuous spherical surface. The mesh for this case was discretized using 100 panels chordwise and 99 panels spanwise with cosine spacing and sharp triangular wing tips at the extremities. Due to unsatisfying results in the tip triangular meshes, which would require more sophisticated surface velocity gradients, the tips were cut off. As these had a limited influence over the rest of the domain, the overall solution was by large unaffected. To approximate the flat plate used in the derivation of the analytical solution, a NACA0012 was selected. A thinner NACA airfoil has been avoided for this analysis due to its susceptibility to numerical errors in the vicinity of the trailing edge, which even XFOIL may struggle with. Since the chord length was elliptically distributed, the thickness also in turn varied throughout the span. The panel code produced the following pressure distribution over the surface of the wing, as per Figure 4-11.

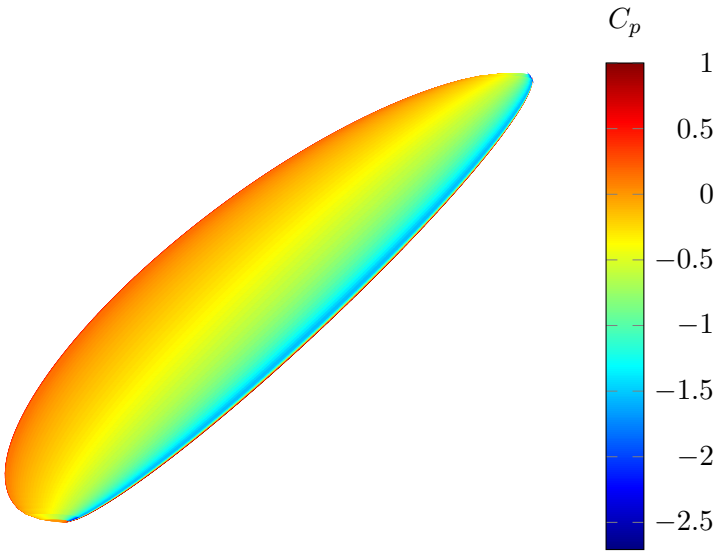

Figure 4-11: Pressure coefficient distribution on suction side for NACA0012 elliptical wing discretized using 100x99 panels with AR $= 10$ in axial flow at $\alpha = 5°$.

The flat plate elliptical wing theory predicts a constant lift coefficient over the wing span. In Figure 4-12a the sectional lift is shown as a fraction of the respective midsection value. The resulting curve shows good agreement with the theoretical solution apart from the tip regions. At the extremities, the wake emission line does not adequately model the flow separation given the curved nature of the tip region, forcing the flow to stay attached in locations where that would not normally be the case. Nonetheless, the circulation plot in Figure 4-12b reconfirms the elliptical spanwise distribution of circulation.

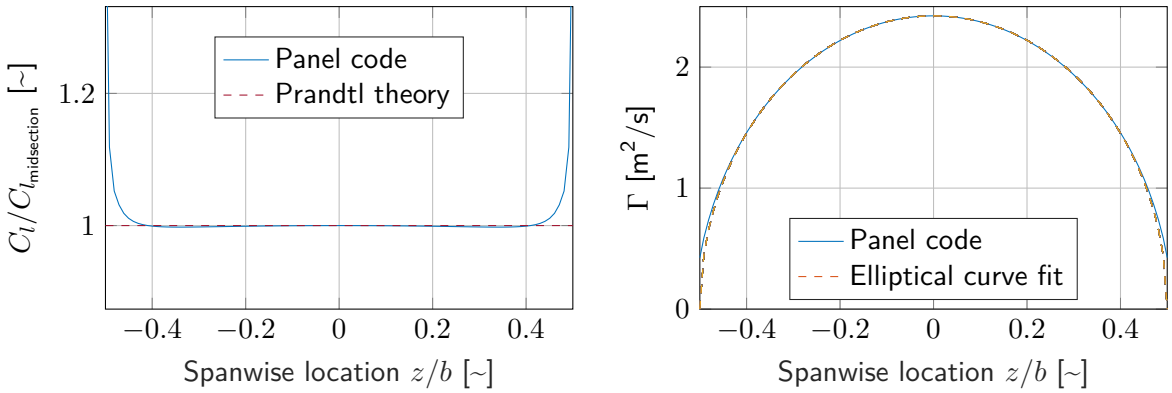

Figure 4-12: Spanwise distribution of sectional lift coefficient as fraction of midsection lift coefficient (a) and circulation (b) for elliptical wing with AR $= 10$, $c = 1$ m in axial flow at $\alpha = 5°$ and $u_\infty = 10$ m/s.

4-6 Rectangular NACA0018 Wing

After full incorporation into AeroModule, the panel code under development is refered to as AWSM3D. The lift coefficient spanwise distribution obtained with the panel code and the lifting line are shown in Figure 4-13 for a rectangular wing with a NACA0018 section profile discretized using 200 panels chordwise and 19 panels spanwise and an AR of 10 immersed in axial flow at an angle of attack of $\alpha = 5°$, using a free wake formulation.

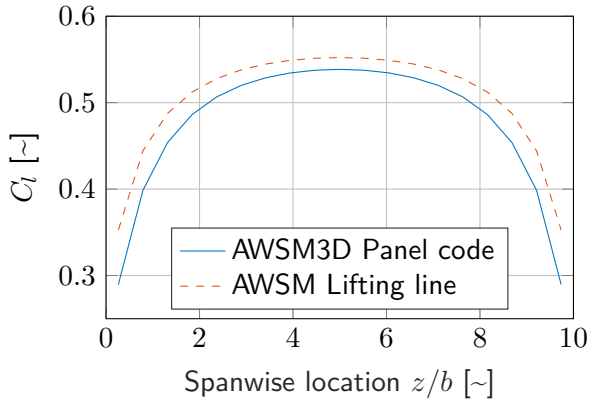

Figure 4-13: Sectional lift coefficient C_l for rectangular NACA0018 with AR $= 10$ in axial flow at $\alpha = 5°$. AWSM lifting line uses inviscid XFOIL polar.

A disparity in magnitude becomes apparent as the AWSM3D indicates lift deficiency compared to the AWSM result, which makes use of inviscid airfoil polars generated with XFOIL. An alternative approach is shown in Figure 4-14, in which AWSM reuses polars generated with AWSM3D operating in quasi-2D conditions. As expected, the two models show good agreement at the midsection where the cross-flows cancel out. In the proximity of the tips, AWSM is shown to generate more lift than AWSM3D. This may be caused by AWSM neglecting the cross-flow which is prominent in the tip region. To reinforce this belief, the discrepancy is observed to grow gradually as the tip regions are approached. While acknowledging this difference, XFOIL polars are used for the remainder of this work to provide for a more holistic validation of AWSM3D.

A sensitivity analysis has been conducted to gauge the influence of aspect ratio onto the lift force generated at the midsection. The results which comprise the panel code, lifting line and XFOIL 2D

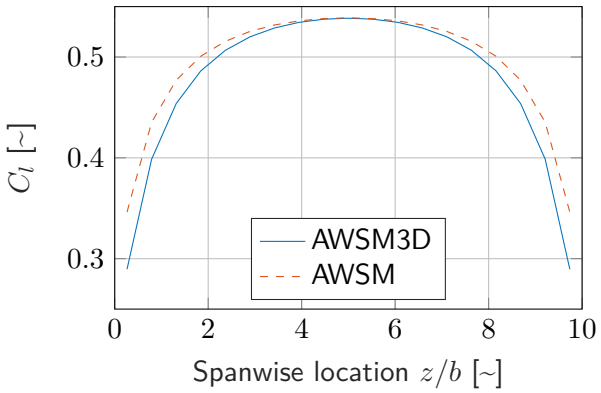

Figure 4-14: Sectional lift coefficient C_l for rectangular NACA0018 with AR = 10 in axial flow at $\alpha = 5°$. AWSM lifting line uses AWSM3D polar.

prediction are included in Figure 4-15. It can be observed that for AR>250 both 3D models visually converge and undershoot the XFOIL solution. Upon further inspection, it is clear that the gap between AWSM3D and AWSM diminishes for higher AR. This may be explained by the non-linear nature of the vortex models, in which local variations in the circulation system propagate to the rest of the system.

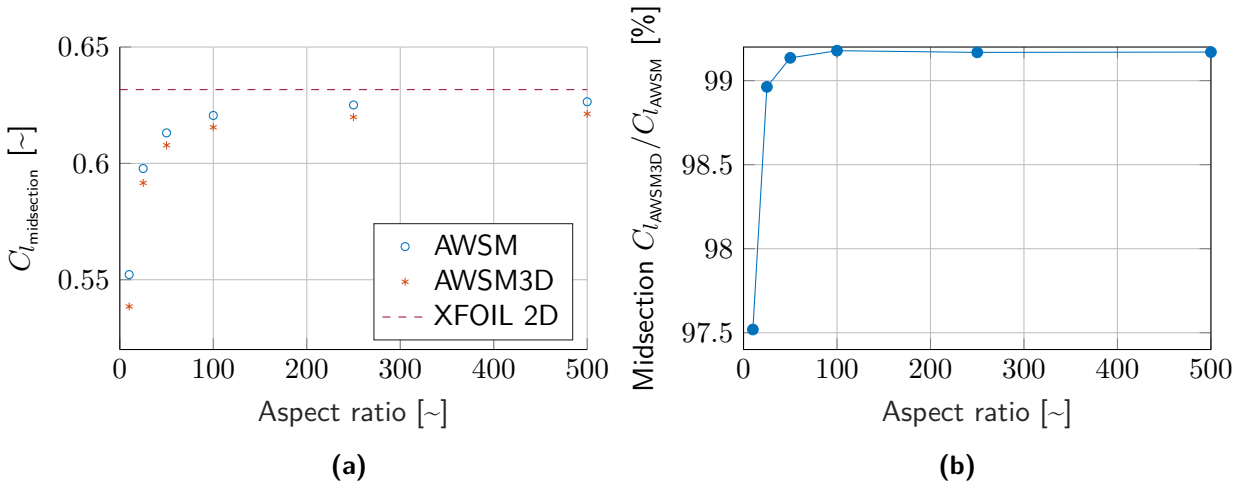

Figure 4-15: Sectional lift coefficient at midspan (a) and respective percentage difference between panel code and lifting line (b) for rectangular NACA0018 wing in axial flow at $\alpha = 5°$. AWSM lifting line uses inviscid XFOIL polar.

4-7 New MEXICO test campaign

In this section, data from the New MEXICO measurement campaign is used. It comprises measurements from two wind tunnel experiment rounds conducted on a 2.25 m radius 3-bladed rotor at DNW (German-Dutch Wind Tunnels), first in 2006 and later revised in 2014 [37, 38]. The cases under consideration involve fully axial inflow, corresponding to tip-speed ratios $\lambda = 10.0$, 6.7, and 4.2, at a rotational speed of 425.1 RPM. The pitch angle is set to -2.3 degrees. The quantity of interest is the pressure measurements taken by sensors placed around the surface of the blade at cross-sections located at 25%, 35%, 60%, 82% and 92% of blade radius.

To assess the validity of the developed panel code, results are compared against an earlier validated panel code. In this sense, the code developed by Van Garrel [7] is employed, which makes use

of a fast novel multilevel integral transform method, coined Multi-Level Multi-Integration Cluster (MLMIC). This method was also validated with experimental MEXICO data and further with a high-fidelity CFD simulation. The geometry under use excludes the nacelle and employs one finely discretized blade with 92 elements radially and 120 elements defining each cross-section, and two coarser blades with 46 radial panels and 30 chordwise panels each. The wake extends 2000 panels from each spanwise emission line.

The AWSM3D simulations make use of a coarser grid, having 32 panels distributed spanwise and 80 panels chordwise per blade. Another major distinction is the blade root cut-off, as the mesh starts at 20% blade radius, as shown in Figure 4-16. This is motivated by current limitations which require a sharp trailing edge, thus blunt trailing edge regions are excluded. The airfoils defining the sections of the blade having a non-zero trailing edge gap were conferred a finite trailing edge using a blending approach implemented in XFOIL.

Design tip speed ratio

The pressure distributions at the 5 spanwise locations are shown in Figure 4-17. Both inviscid panel codes show very good agreement on the three most outboard sections. The section at 25% radius however exhibits a relatively significant discrepancy, which may be attributed largely to the difference in the geometry under consideration, particularly in the root region. Compared to the geometry used by van Garrel in the case of AWSM3D, the 25% radius section is located closer to the root cut-off, which implies that the root vortex has a larger influence on the flow around this section, thereby causing an undershoot in the pressure difference. The main factor behind the discrepancy of the panel codes and the experimental data is viscosity, which is not accounted for in the inviscid models. Closer to the tip the viscous effects diminish, bringing the three curves closer as seen at the 82% and 92% radius stations.

High tip speed ratio

The high tip speed ratio case is displayed in Figure 4-18. Apart from the 25% radius station, the panel codes match reasonably well except for the suction side at 82% and 92%. Remarkably, these regions are known to attract the least viscous influence, given their proximity to the tip. Additionally, the high tip speed ratio indicates a further decrease in viscosity. Therefore, the panel codes are expected to show better agreement with the experimental data in this particular case. For these reasons, AWSM3D is found to perform better at these locations.

Low tip speed ratio

The pressure distributions for the low tip speed ratio are presented in Figure 4-19. Viscosity plays a larger role here, which explains the larger difference between the panel codes and the experimental measurements. The panel codes match remarkably well for the most part, showing a minor discrepancy around the suction peak at 60% radius.

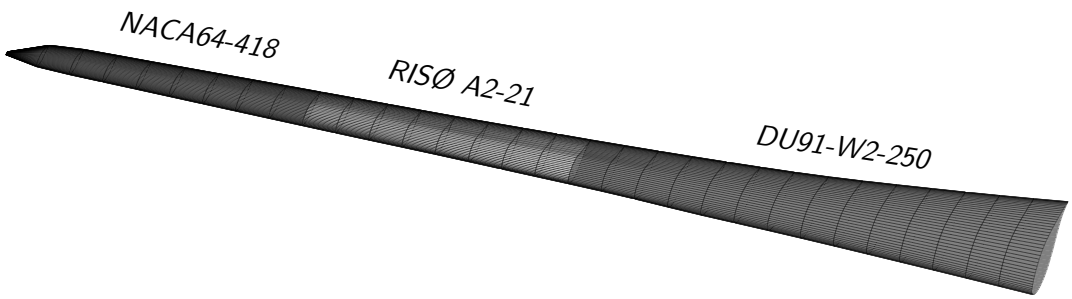

Figure 4-16: MEXICO mesh geometry used in AWSM3D simulation.

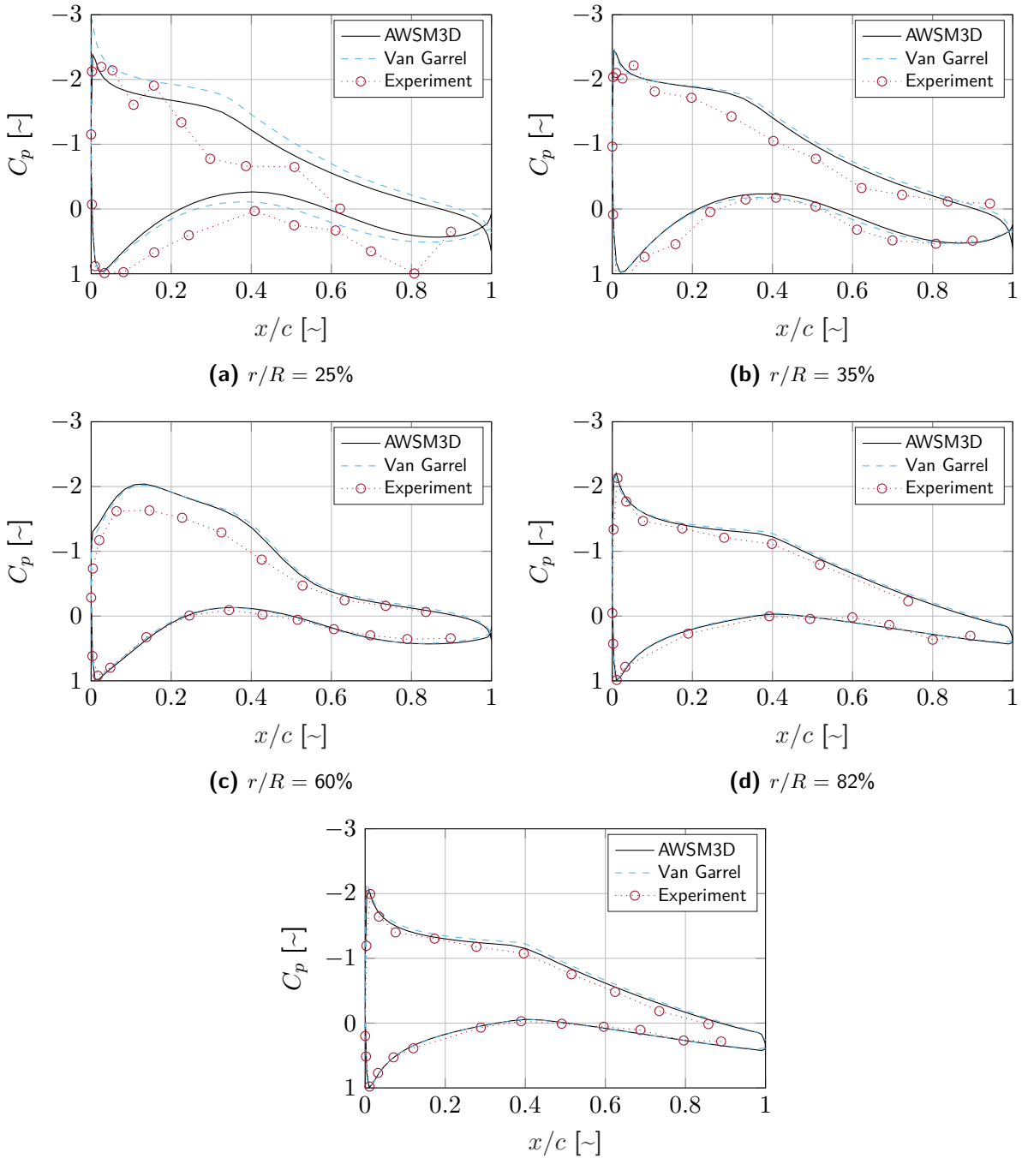

(a) $r/R = 25\%$

(b) $r/R = 35\%$

(c) $r/R = 60\%$

(d) $r/R = 82\%$

(e) $r/R = 92\%$

Figure 4-17: New MEXICO rotor pressure coefficient distribution operating in axial flow at design tip speed ratio $\lambda = 6.8$, inflow velocity $u_\infty = 14.7$ m/s, pitch angle $= -2.3°$.

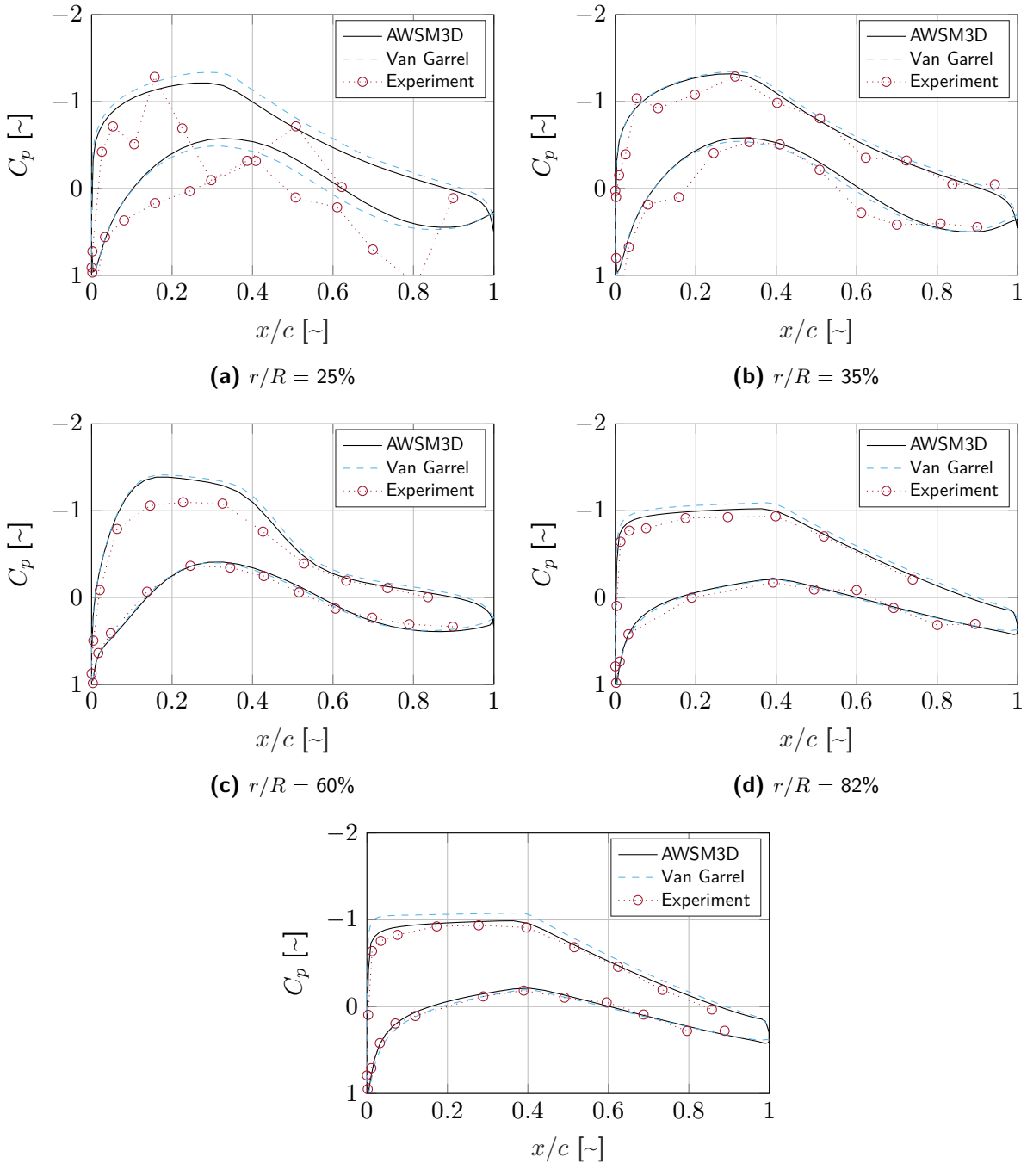

(a) $r/R = 25\%$ **(b)** $r/R = 35\%$

(c) $r/R = 60\%$ **(d)** $r/R = 82\%$

(e) $r/R = 92\%$

Figure 4-18: New MEXICO rotor pressure coefficient distribution operating in axial flow at high tip speed ratio $\lambda = 10.0$, inflow velocity $u_\infty = 10.0$ m/s, pitch angle $= -2.3°$.

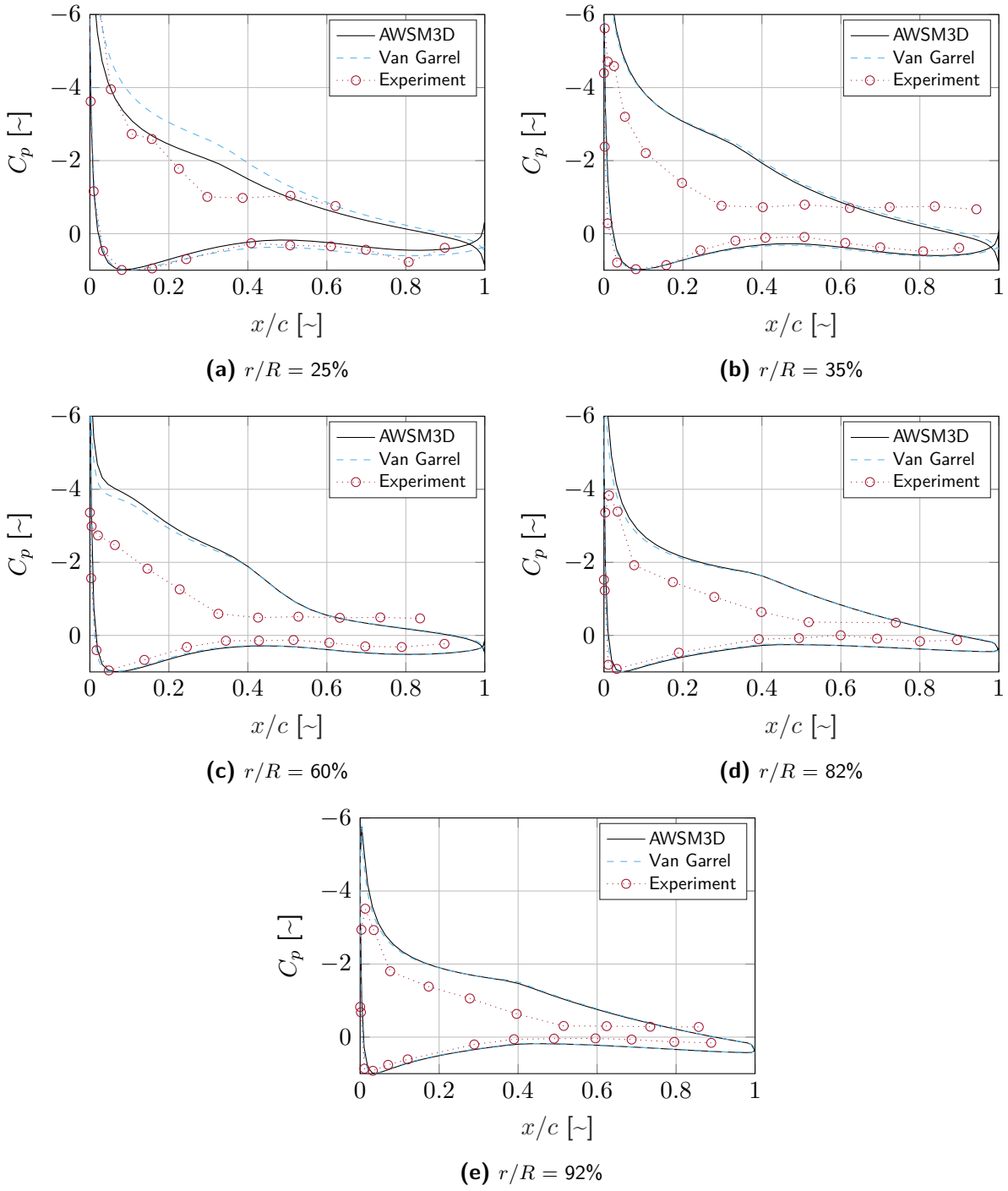

(a) $r/R = 25\%$

(b) $r/R = 35\%$

(c) $r/R = 60\%$

(d) $r/R = 82\%$

(e) $r/R = 92\%$

Figure 4-19: New MEXICO rotor pressure coefficient distribution operating in axial flow at low tip speed ratio $\lambda = 4.2$, inflow velocity $u_\infty = 24.1$ m/s, pitch angle $= -2.3°$.

Chapter 5

Results

Chapter 5 delves into the characteristics of the flow passing around a swept turbine blade geometry by analyzing the results of the simulations run with the AWSM3D developed code. Having validated the developed panel code with conventional test cases, the initial focus shifts to validating the model for swept geometries, to the extent to which it is possible. Aiming to decouple the effect of sweep from more complex phenomena and interactions, the starting test involves a simple rectangular fixed wing. The latter is swept using two commonly used methods, namely by bending or shearing the original blade. The panel method results are thereafter compared against established theory and its lifting line counterpart for both a fore- and aft-swept wing.

Increasing in complexity, a baseline unswept version of the IEA 15-MW reference wind turbine is used for further study of sweep. First, the results for the baseline blade are obtained for the developed panel code, the lifting line model, and an established panel code. Lastly, the blade is swept according to a given sweep parametrisation that includes both a fore- and aft-swept blade setting. These geometries are ultimately used to conduct a rigorous assessment of the capabilities of a lifting line model and a panel code in what concerns predicting the flow around a more complex wind turbine swept geometry in conditions resembling its typical operating envelope.

5-1 Rectangular wing

In this section, a simple rectangular wing is proposed to analyze the effect of sweep on flow aerodynamics. To better isolate the effect of sweep from more complex flow phenomena, such as those arising from finite wings, a high aspect ratio of 250 is selected. A high aspect ratio may preserve the 2D nature of the flow, particularly in the center region of the wing, which may thereby bridge the gap between the lifting line and the panel code simulations. Additionally, the two sweeping techniques covered in subsection 5-1-1 result in distinct shapes at the two extremities, which may lead to diverging solutions locally. A high AR may therefore ensure that these local distortions do not propagate far inboard. The remaining parameters of this test case are provided in Table 5-1.

First, the panel code solution is evaluated for the two sweep methods proposed in subsection 5-1-1. An assessment of said solution is provided to establish the suitability of the panel code to resolve the two configurations, using the cross-flow principle theory as benchmark. This is followed by an analysis and comparison of the panel code and lifting line solutions for both backward and forward swept wing geometries in subsection 5-1-2.

Table 5-1: Rectangular wing case properties.

Parameter	Setting
Airfoil	NACA0018
Chord c	1 m
AR (straight)	250
Sweep angle λ	$\pm 45°$
Angle of attack α	5°
Flow velocity U_∞	15 m/s

5-1-1 Sweep methods

The two methods of sweeping a wing commonly employed in literature are by means of bending or by shearing the sections. Both methods are visualized in Figure 5-1. In the bent configuration, the airfoil sections remain normal to the leading edge. This is equivalent to a straight wing which is yawed with respect to the incoming flow. The sweep angle λ in this case coincides with the yaw angle and is constant along the span. The sheared variation of the swept blade can be obtained by shearing each subsequent section along the chord line, such that the airfoil sections remain parallel to their straight wing counterparts. These techniques ultimately produce distinct geometries. Lastly, in classic wing aerodynamics that involve practical experimental setups, the wing is often swept in a way that keeps the root chord in its original location, combined with potential smoothening of the geometry at the tip. For the sake of this analysis, the geometry is kept as two-dimensional as possible and therefore no further modifications are applied.

As a result of sweeping a wing by bending, or equivalently yawing the wing, the chord length parallel to the freestream varies by a factor $\cos^{-1}\lambda$. Therefore, to recreate the same geometry using a sheared approach, in which the chord is defined in flow direction, the airfoil sections must be elongated accordingly, while preserving the thickness. This implies that the swept geometry (t/c) ratio, defined in streamwise direction, varies by a $\cos\lambda$ factor. Following the analysis carried out in [3], given that the streamlines over a swept wing mostly follow along the chord defined in flow direction, this essentially leads to $c_p \propto (t/c) \propto \cos\lambda$. The latter relation then lays the groundwork for the application of the cross-flow principle corrections for swept flows.

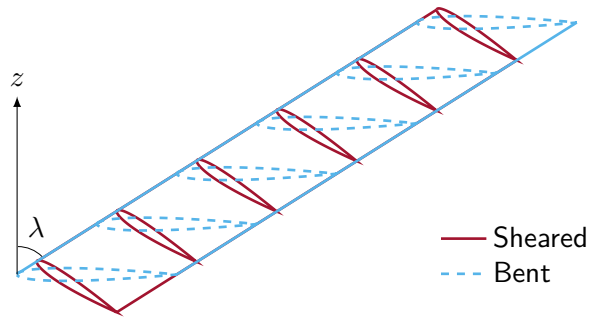

Figure 5-1: Sweep variations.

Besides the aforementioned chord varying with the extent of sweep, the wingspan normal to the incoming flow also changes by a factor $\cos\lambda$. Assembling these effects together results in the AR

varying by a factor $\cos^2 \lambda$. For the case at hand, a $\lambda = 45^\circ$ reduces the AR from 250 for the straight wing to 125 for the swept case. As concluded in section 4-6 for the same geometry in a straight configuration, the seemingly abrupt drop in AR should nonetheless lead to minimal distortion of the solution in the mid-section.

In conjunction with the geometrical properties of Table 5-1, the AWSM3D simulation settings listed out in Table 5-2 are used to solve the flow for the two versions of the swept blade. Even though the cross-sections are described by two distinct airfoil profiles, the two geometries are identical except at the extremities. The circulation system attached to the surface of the two meshes have similar distributions, apart from two notable differences. First, the orientation of the chordwise edges of the doublet and source elements varies, and second, the spanwise edges are offset in spanwise direction. The wake emission line is shared across the two cases. The total (wetted) surface area is the same, as is the area of each individual panel. For these reasons, the choice of a sweep method itself, which leads to a particular setup of the bound circulation system, should not be pertinent as long as numerical errors are negligible.

Table 5-2: Sweep variation case AWSM3D settings.

Parameter	Setting
Number of panels	Chordwise: 250 Spanwise: 20
Panel spacing	Cosine
Timestep	0.1 s
Number of timesteps	800
Wake type	Free

The sectional lift coefficient and circulation for the two variations of sweep are shown in Figure 5-2. The lift coefficient in Figure 5-2a for the straight wing at the midspan compares to the XFOIL value in a similar manner as it was seen in section 4-6. The bent configuration shows very good agreement in the mid-section with the cross-flow principle curve, which was obtained by applying the $\cos \lambda$ sweep correction factor to the straight wing curve. As the cross-flow correction is derived for a 2D case, the match is worse close to the extremities due to local prevalence of 3D phenomena. The sheared case exhibits a severe discrepancy comparing to the other swept curves. Despite this, the circulation plots in Figure 5-2b of the three configurations all match reasonably well, with the two swept curves coinciding for the most part.

Although the circulation in both swept configurations has the same orientation and magnitude, the c_l curves do not match accordingly even though the reference area is identical. It becomes apparent that an error has been introduced in the processing of the circulation solution to extract the aerodynamic loads. The intermediate steps between the two are the determination of the surface flow velocity conducive to the computation of the pressure distribution and subsequent non-dimensionalization of resulting pressure loads, which has an associated reference area.

Surface velocity computation algorithms are notorious for being one of the largest sources of modeling errors in panel codes. In this instance, it appears that the current algorithm in place is inadequate for resolving the surface doublet distribution gradient on the non-orthogonal mesh present in the sheared case. Upon closer inspection of said gradients, an error was ascertained, however not one that would account for the entire discrepancy. Additionally, the reference area may need a revamped definition to account for mesh non-orthogonality. In further analysis, only the bent formulation of sweep is considered.

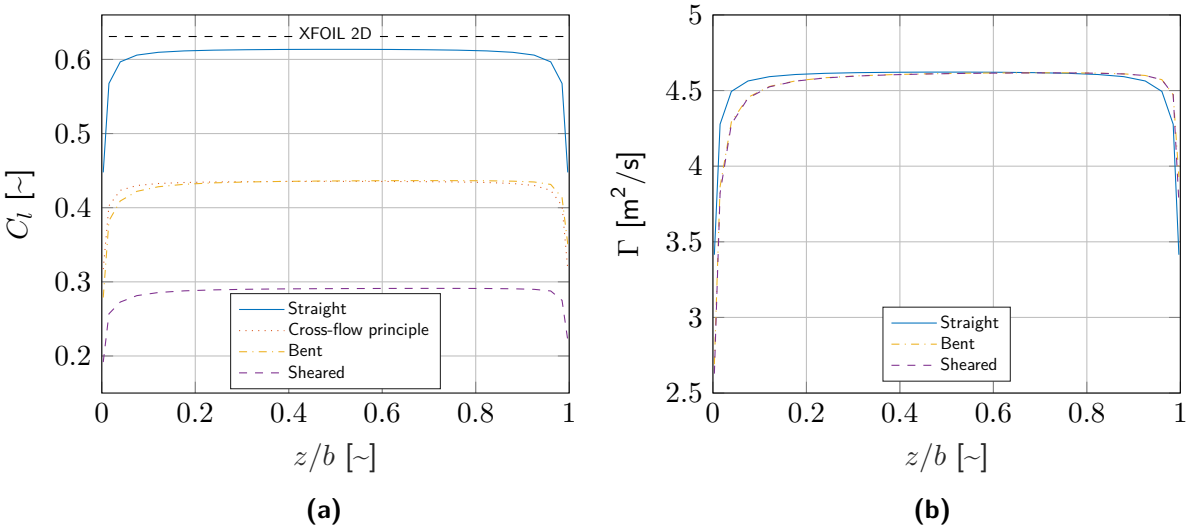

Figure 5-2: Lift coefficient (a) and circulation (b) for a NACA0018 rectangular wing with AR = 250 at angle of attack α= 5° for a straight and bent/sheared planforms with sweep angle λ= 45°.

5-1-2 Swept wing flow analysis

As seen in subsection 5-1-1, the effect of sweep is manifested through two distinguishable mechanisms, namely a 2D magnitude correction covered by the cross-flow principle theory and a predominantly 3D effect produced by the presence of a wake. In this section, these effects are dissected by examining the flow over the geometry described in Table 5-1, to which a bent type of sweep is applied, and the simulation settings of Table 5-2 are used. For the above parameters, equivalent AWSM lifting line simulations have been devised and prepared for comparison. These use inviscid airfoil polars generated with XFOIL.

The AWSM3D panel code and AWSM lifting line results for an aft swept blade are compiled in Figure 5-3. For consistency, the cross-flow sweep correction has been applied separately to each model's straight configuration result. Examining Figure 5-3a, both models show a close match to the cross-flow theory at the midspan.

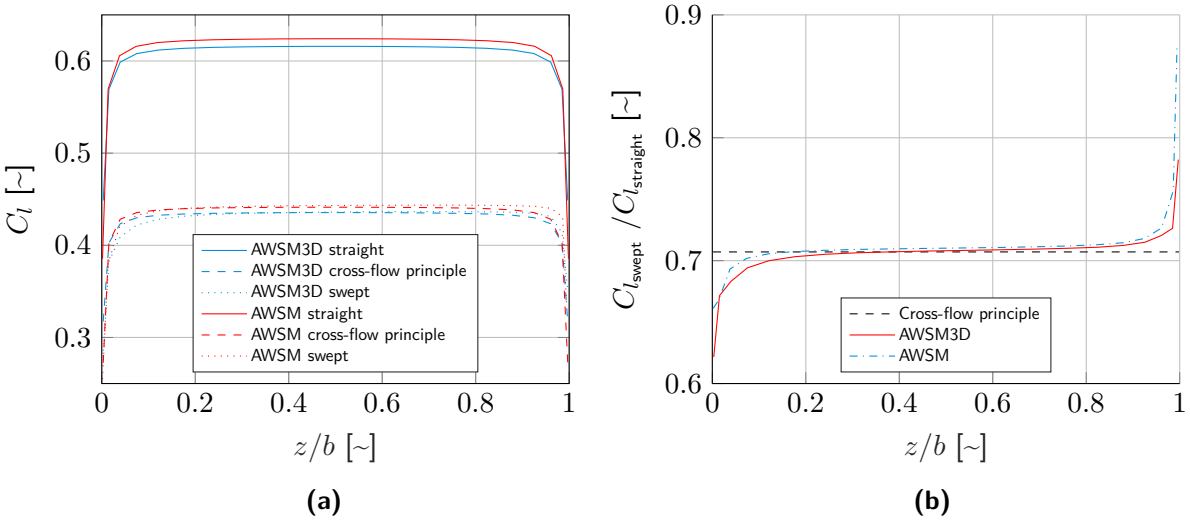

Figure 5-3: Lift coefficient (a) and ratio of swept to straight lift coefficient (b) for a NACA0018 rectangular wing with AR = 250 at angle of attack α= 5° aft swept with sweep angle λ= 45°.

Figure 5-3b indicates the ratio between the swept and straight wing lift coefficient for each respective

model. The effect of sweep is predicted remarkably well by cross-flow principle theory for both models in the mid-section. The aft swept end of the wing has a higher loading than the midsection, while the opposite holds for the fore swept end. As expected, due to the 2D nature of the cross-flow correction, it falls off at the ends where the wake influence is at large.

Upon further inspection the asymmetry of the loading can be ascertained, which is again a consequence of the presence of a wake in the swept flow case. The relative orientation of the wake, which is aligned with the freestream direction, to the bound circulation creates less downwash at the aft swept end than at the fore swept extremity. The method proposed by Fritz *et al.* [39] to model the effect of sweep is to superimpose onto a straight wing the contribution of a straight vortex filament to account for this variation in induced velocities. The method proposed by Fritz corroborates well with the results of the LL and the panel code in predicting that the missing vortex filament on the aft swept end induces an upwash locally. The vice-versa applies to the fore swept end, however it is not necessarily mirrored, likely due to the non-linearity of the model. The aforementioned upwash is reflected in the loading overshoot of the codes seen in Figure 5-3b. The panel code results exceed the cross-flow curve starting with the 40% span position, whereas the LL already overshoots starting as early as ≈20% span, measured from aft swept end.

Figure 5-4 is added for completeness to showcase the loading on a fore swept wing. As expected, the results are mirrored compared to the aft swept wing. Note that AWSM lifting line code does not allow for a non-zero sweep angle on the first element at the root. For that reason, the last data point on this figure and the first one on Figure 5-3 are inaccurate.

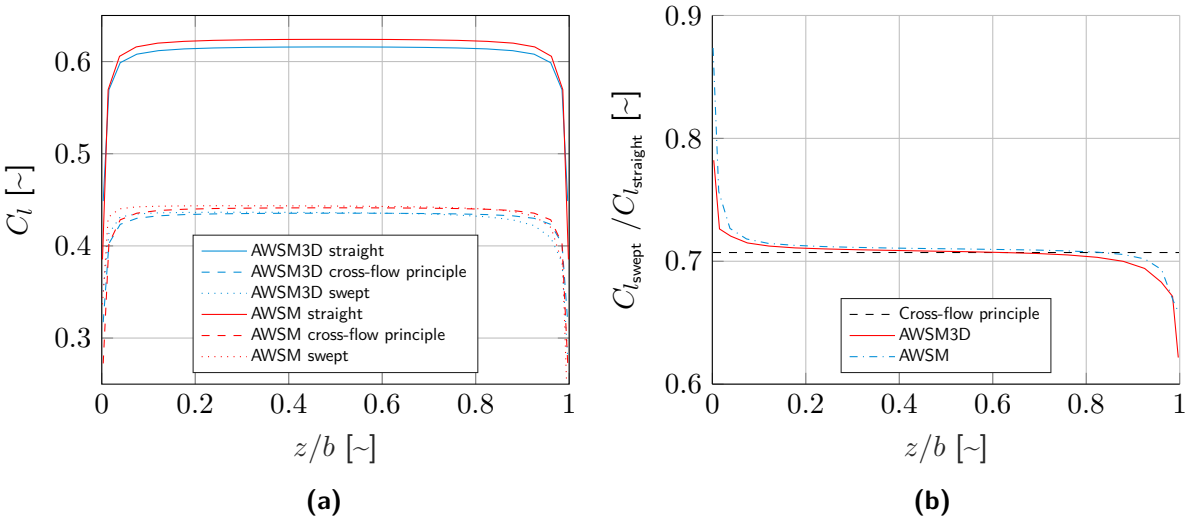

Figure 5-4: Lift coefficient (a) and ratio of swept to straight lift coefficient (b) for a NACA0018 rectangular wing with AR = 250 at angle of attack α= 5° fore swept with sweep angle λ= 45°.

Overall, the two models show good agreement with each other, and convincingly reaffirm the cross-flow theory correction, particularly around the mid-section. The spanwise load asymmetry is slightly more pronounced in the LL results. Lastly, the two models do display higher levels of variance in the immediate proximity of the tips, where the flow regime is dominated by the tip vorticity. In confirmation of the findings of section 4-6, in the presence of cross-flow induced by tip vortices, the panel code shows deficient lift in comparison to the LL.

To illustrate the effect that the orientation of the wake with respect to the wing has on the aerodynamics a further simplified case is provided as represented in Figure 5-5. The spanwise discretization is reduced to a single element extending from tip to tip, thereby neglecting the spanwise variation of circulation and introducing/discharging the circulation via the strong trailing vortex filaments. To allow for easy visualization, a fixed wake structure aligned with the incoming flow is assumed where the starting vortex has already vanished downstream. It can be observed that the yawed

inflow induces an asymmetry due to the relative orientation of the two trailing vortex filaments. By decomposing the influence of the vortex filaments into components normal and parallel to the wing's span axis, it can be observed that the parallel component of the trailing filament located in the vicinity of the aft swept end of the wing induces an upwash at locations along the wing, whereas the opposite holds for the fore swept end. Furthermore, on the aft swept tip of the wing a region with a resultant upwash can also be identified, especially closer to the leading edge/tip corner. With a more finely discretized setup this effect is expected to propagate throughout the wing.

The orientation of the wake does not only prescribe a sign for the velocity induced by it but also has an effect on its magnitude as per the Biot-Savart evaluation. This effect is not as easily discernible by visual inspection, but it can be seen that overall the yawed inflow results in the wake being closer to the wing. The resulting flow for a more accurate representation of this case using a free wake with a finer discretization is far more difficult to predict. Comparing the panel code and the LL simulations in view of these modifications does not yield any new notable differences or limitations for either model compared to a conventional straight wing. It could be argued that the cross-flow induced specifically by the wake is reduced as a result of its skewed orientation when compared to a straight wake. Nonetheless, this is countered to an extent by the addition of the cross-flow component of the inflow itself, which is also skewed.

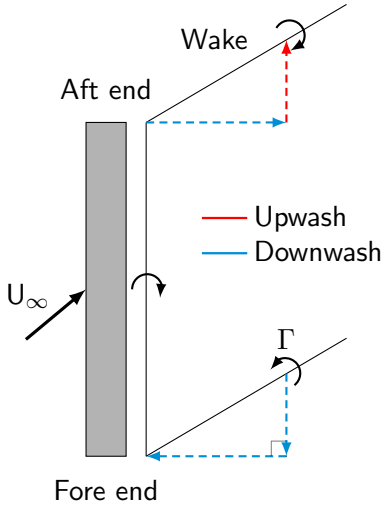

Figure 5-5: Yawed wake decomposition.

To further investigate the implications of sweep, the wake structure is examined. To facilitate visualization, a reduced AR=5 is used and a larger timestep of 1 s is instated. The latter is selected such that the root and tip vortex roll-up is minimized along a further distance downstream. A lower temporal resolution may thus delay such phenomena that are not pertinent to this analysis. The resulting wake structure and its circulation can be observed in Figure 5-6. The asymmetry can be observed in the development of the wake too, as the free wake is pulled upstream on the aft swept side whereas on the fore swept side it is pushed further downstream. Similarly, the higher circulation on the aft swept end leads to more downwash on nearby wake.

5-2 IEA 15-MW reference wind turbine

The last step in analyzing the effect of sweep undertaken in this work is to simulate the IEA 15-MW reference wind turbine. Among the complexities introduced in this test case are the inclusion of sweep variation along the span, variable twist and rotation. First, a description of the setup of the simulations is provided. An initial set of simulations is run to check the baseline turbine AWSM3D results against the AeroModule's BEM and LL models, as well as against Vortexje. Lastly, the results for the fore and aft swept turbine blades are presented and analyzed.

5-2-1 Geometry description

The baseline IEA 15-MW reference turbine blade defined in [12] was used. A number of modifications were applied, as listed below, to tailor the geometry to the purposes of this work. To minimize unwanted interactions, a few parameters such as the precone angle, tilt angle, and prebend were set to 0. Additionally, the cylindrical root region and the transition pieces up until the first discrete

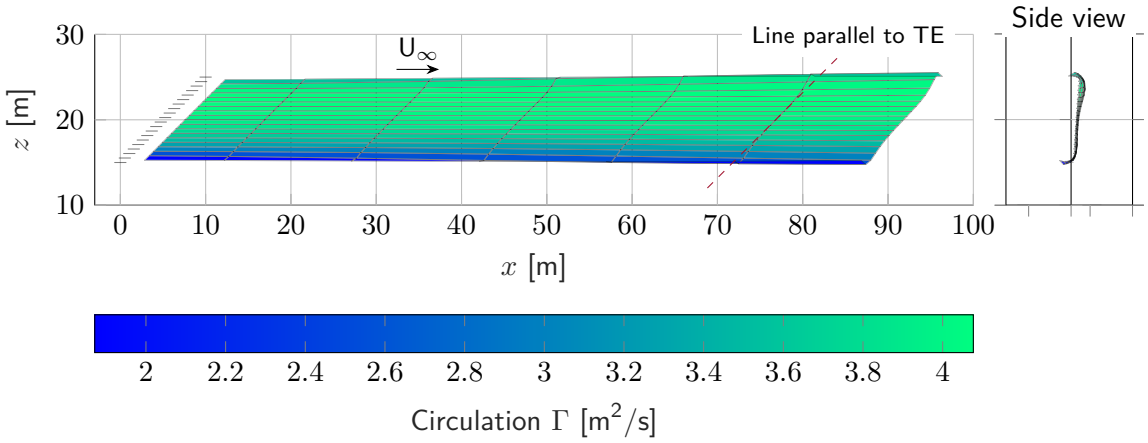

Figure 5-6: AWSM3D wake circulation for NACA0018 with AR = 5 at angle of attack α= 5° with sweep angle λ= 45°.

airfoil can be distinguished are cut off in a manner similar to the New MEXICO geometry treatment in section 4-7. The relevant list of parameters is included in Table 5-3.

The airfoils used in the IEA 15-MW reference turbine blade are displayed in Figure 5-7. To ensure sufficient modeling precision, a set of blended airfoils is also supplied. These serve as intermediate profiles to be located between the main airfoils. The finite thickness trailing edges detailed in the turbine definition report suggest flatback airfoils, which fall outside the current possibilities of the developed panel code. The workaround for this limitation involves sharpening the trailing edge in its vicinity. To this end, a tool packaged with XFOIL was employed, which made use of a blending length approach that only modified the profile locally. The original airfoil profile is shown in the same figure with a dashed line.

Special care was taken such that in modifying the profiles the flow characteristics would not deviate excessively from the original. To ensure this, the simple 2D inviscid panel code results of XFOIL were used. After careful inspection of the pressure distribution around the cross-sections, the difference due to the modifications in question was largely contained at the trailing edge. In the rest of the chapter, all simulations are run using these sharpened profiles.

Another model limitation that hinders the quality of aerodynamic results is related to the presence of cusped trailing edges, especially prominent for the FFA-W3-241 and FFA-W3-211 airfoils in Figure 5-7d and 5-7e. This mainly affects the numerical stability of the solution, caused by the system of equations becoming singular, as hinted by Morino and Kuo [40]. This is a common struggle for panel codes, manifested through a cross-over in the pressure graph at the TE [41]. Two remedies for this issue are offered by Yon *et al.* [42]. One concerns adjusting the size of the panels at the trailing edge and their angles, i.e. by coarsening the grid at the trailing edge. The second option is to use a Neumann boundary condition at the trailing edge in combination with the usual Dirichlet

boundary condition applied over the rest of the body. In the latter case, the flow velocity over either side of the trailing edge is set to be equal.

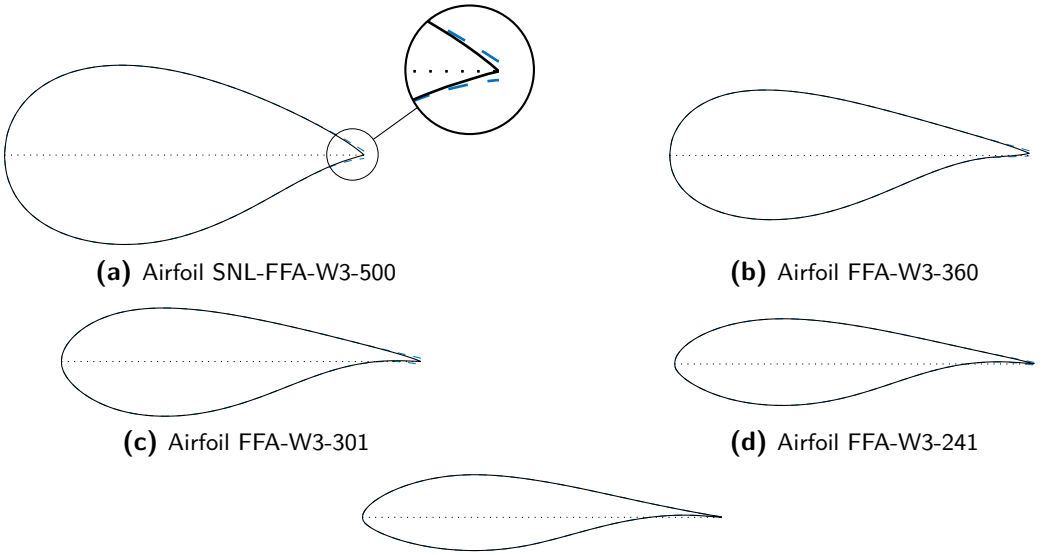

(a) Airfoil SNL-FFA-W3-500

(b) Airfoil FFA-W3-360

(c) Airfoil FFA-W3-301

(d) Airfoil FFA-W3-241

(e) Airfoil FFA-W3-211

Figure 5-7: Airfoils describing IEA 15-MW reference turbine cross-sections [12].

Table 5-3: IEA15MW reference turbine blade main characteristics.

Parameter	Setting
Number of blades	3
Rotor diameter	240 m
Blade prebend	0 m
Root radius	17.1 m
Precone angle	0 deg
Tilt angle	0 deg
Pitch angle	0 deg

5-2-2 Baseline results

As a first step, the baseline configuration of the IEA 15-MW reference wind turbine was analyzed with the solvers included in AeroModule (AWSM3D, AWSM, BEM) and additionally with the panel code Vortexje. The panel codes were supplied with the same identical mesh, whereas the LL generated an equivalent blade containing the same number of spanwise elements and used XFOIL generated inviscid airfoil polars. The simulation settings are listed in Table 5-4.

The baseline results are shown in Figure 5-8, containing the set of forces normal (axial) F_{ax} and tangential F_{tan} to the rotor plane, in standard Vortexje output format. In this particular instance, the BEM and AWSM3D results match well, whereas AWSM predicts larger forces. This is in line with the findings of section 4-6, which relates the observed discrepancy to the use of XFOIL polars.

Table 5-4: IEA15MW simulation settings.

Parameter	Setting
Number of panels	Chordwise: 50 Spanwise: 60
Panel spacing	Cosine
Timestep	0.2328 s
Rotor speed	7.162 RPM
Azimuthal step	10 deg
Wake size	10 revolutions
Wake type	Free
Flow velocity U_∞	10 m/s

A more drastic drop in load can be observed for Vortexje, for which the explanation falls outside the scope of this thesis. For these reasons, Vortexje is excluded from further analysis.

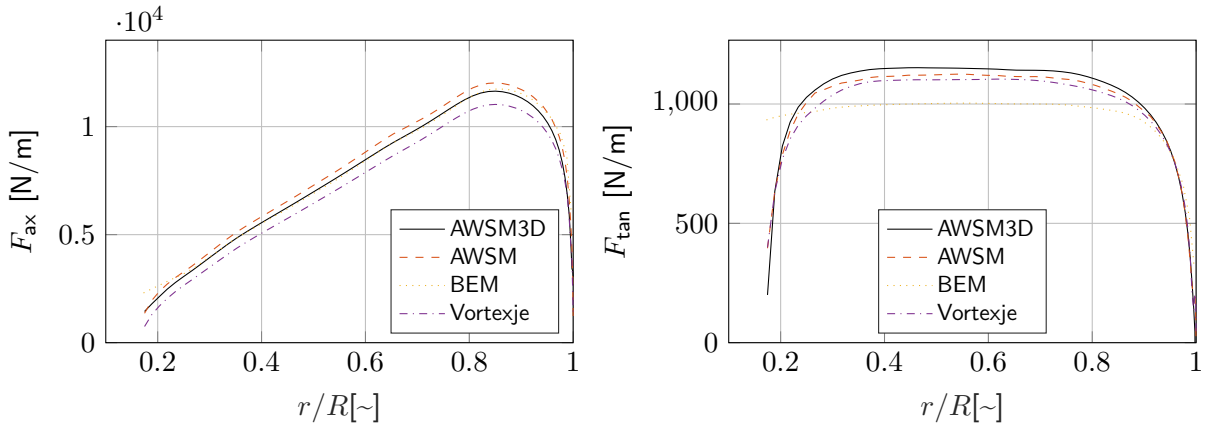

Figure 5-8: Axial and tangential to rotor plane forces acting on baseline IEA15MW turbine blade.

To further validate the results, the same configuration was rerun with a pitch angle of 8 degrees, as shown in Figure 5-9, which depicts the chord-normal (F_n) and chord-tangential (F_t) force distributions, in customary AeroModule output format. As established by Schepers *et al.* [43], the AeroModule AWSM and BEM simulations show better agreement at lower induction factors (<0.3), such as in this case. AWSM3D is again shown to generate less force.

5-2-3 Swept geometry

The parameters used in the definition of sweep are shown in Table 5-5, following the method outlined in Equation 2-2, albeit with a change in coordinate frame as per Equation 5-1. This set of parameters follows from Fritz *et al.* [39], applying for $y > y_{start}$.

$$x = x_{tip}\left(\frac{y - y_{start}}{L_{Blade} - y_{start}}\right)^{\gamma} \tag{5-1}$$

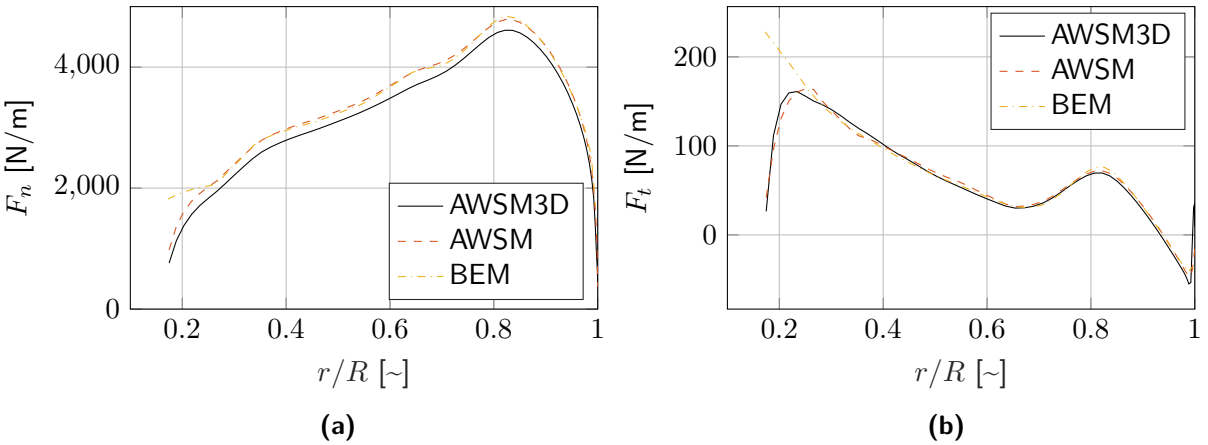

Figure 5-9: Chord-normal (a) and tangential (b) forces acting on baseline IEA15MW turbine blade in low a configuration.

Table 5-5: IEA15MW sweep parametrisation.

Parameter	Setting
y_{start}	$0.5R$
x_{tip}	$\pm 0.2R$
γ	2

The ensuing planform shape modifications can be examined in Figure 5-10. Following the bent sweep approach, the applied sweep is accompanied by a rotation of the local airfoil, preserving the baseline local section orientation with respect to the local blade pitch axis. The swept configuration is scaled by a factor $\frac{1}{\sqrt{1+x_{tip}^2/R^2}}$ such that the resulting geometry has the same tip radius as the baseline blade.

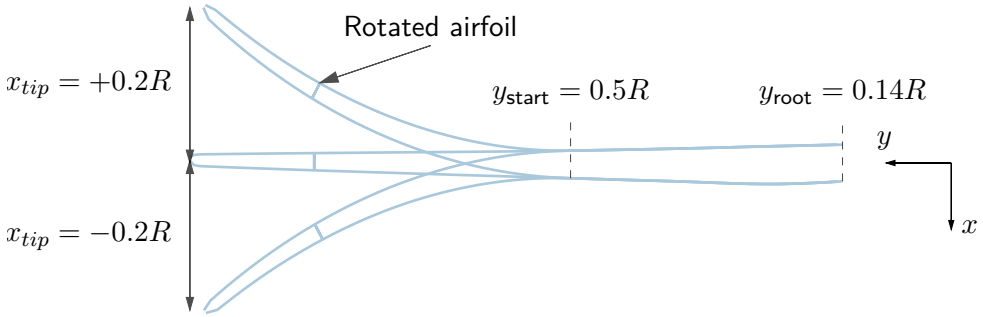

Figure 5-10: IEA 15-MW baseline and swept case geometries.

Aft swept geometry

The aggregated results for the backward swept geometry for the panel code and lifting line simulations are shown in Figure 5-11. At first glance, both simulations exhibit the same behavior in the swept region. To better visualize the variation in normal force caused by the applied sweep, each

curve is compared separately against the cross-flow principle correction factor applied to each case respectively as per Figure 5-12.

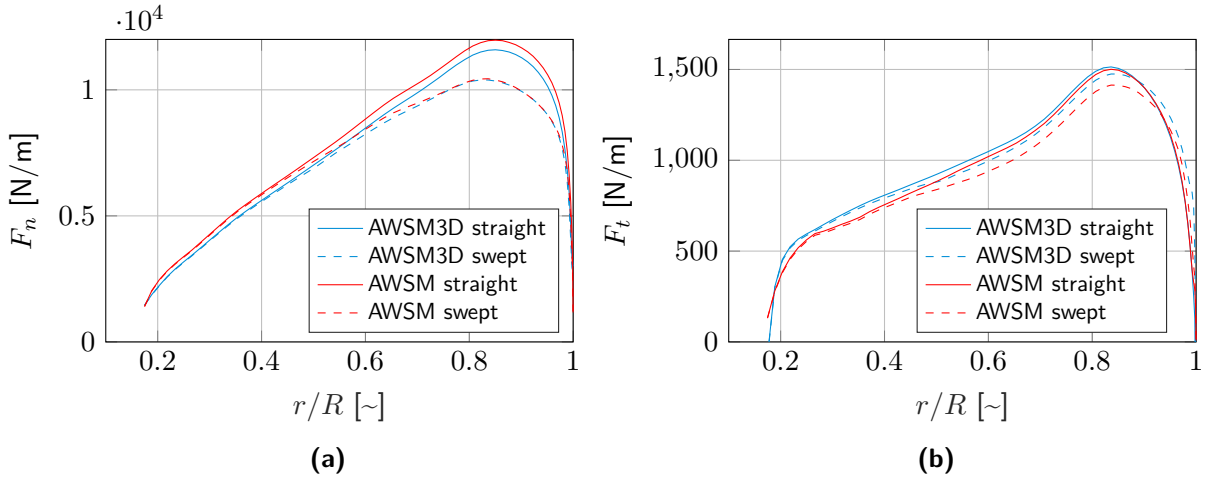

Figure 5-11: Chord-normal (a) and tangential (b) forces acting on baseline and aft swept IEA15MW turbine blade.

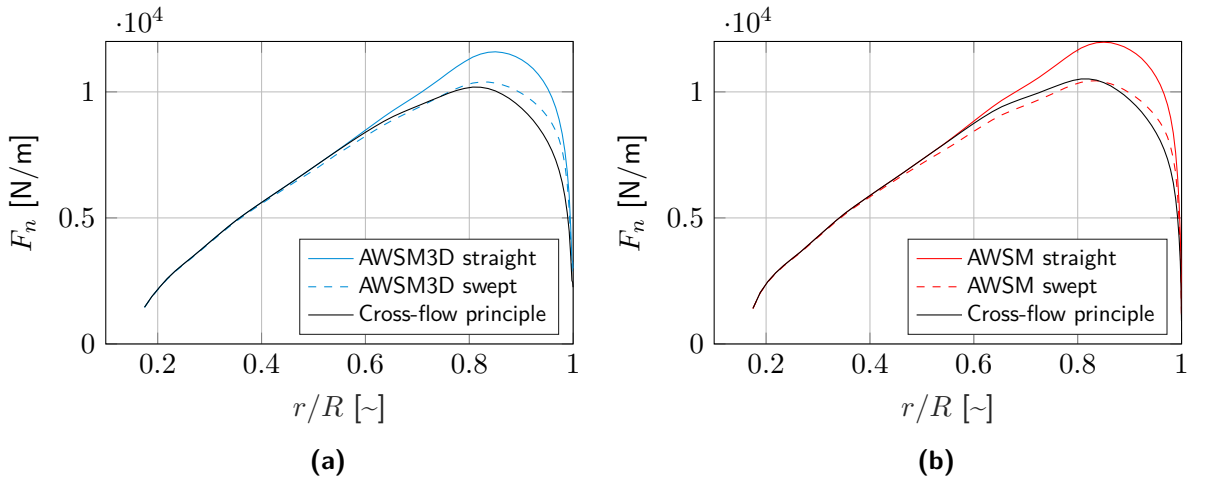

Figure 5-12: AWSM3D (a) and AWSM (b) chord-normal forces acting on baseline and aft swept IEA15MW turbine blade.

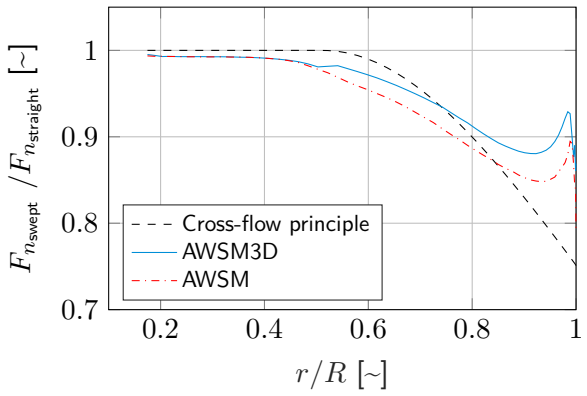

Figure 5-13: Aft swept blade chord-normal force fraction of straight configuration chord-normal force.

Upon inspection, both the AWSM and AWSM3D results abide well by the cross-flow correction curve considering the overall drop in force. Next to that, the spanwise deviation from it is consistent with the findings of subsection 5-1-2. A spanwise redistribution of the loading occurs, visibly starting earlier than the point of application of sweep at $r \approx 0.5R$. In both instances, the tip region experiences elevated loads while the midspan exhibits a slight drop in force when compared to the cross-flow curve.

A comparison between the two models and the cross-flow correction is presented in Figure 5-13. Traces of an undershoot in force with respect to the cross-flow curve can be noticed in the unswept region for both simulations from the very root. In the vicinity of the region where sweep is first introduced ($r \approx 0.5R$), a slight kink is present in the AWSM3D curve, something that does not entirely seem physical and may indicate a simulation error. The same artifact has been noticed in a more pronounced state in results obtained with Vortexje for the same geometry, which would warrant an investigation into panel code behavior in this region. Up until $r \approx 0.8R$ both models exhibit lower forces than the cross-flow principle curve predicted, with the AWSM3D results surpassing the cross-flow curve slightly earlier than AWSM. Similarly, in the entirety of the domain, the AWSM3D curve is higher than its AWSM counterpart in comparing the relative drop from their respective straight baseline results.

Fore swept geometry

The same analysis has been conducted for a forward swept geometry with $x_{tip} = +0.2R$, the results of which are shown in Figure 5-14. Similarly, the normal force results of the two simulations were separated to visualize their respective comparison to the cross-flow principle correction curve in Figure 5-15. Again, the cross-flow correction predicts the overall decrease in aerodynamic load reasonably well, although it does overpredict it, particularly in the case of AWSM.

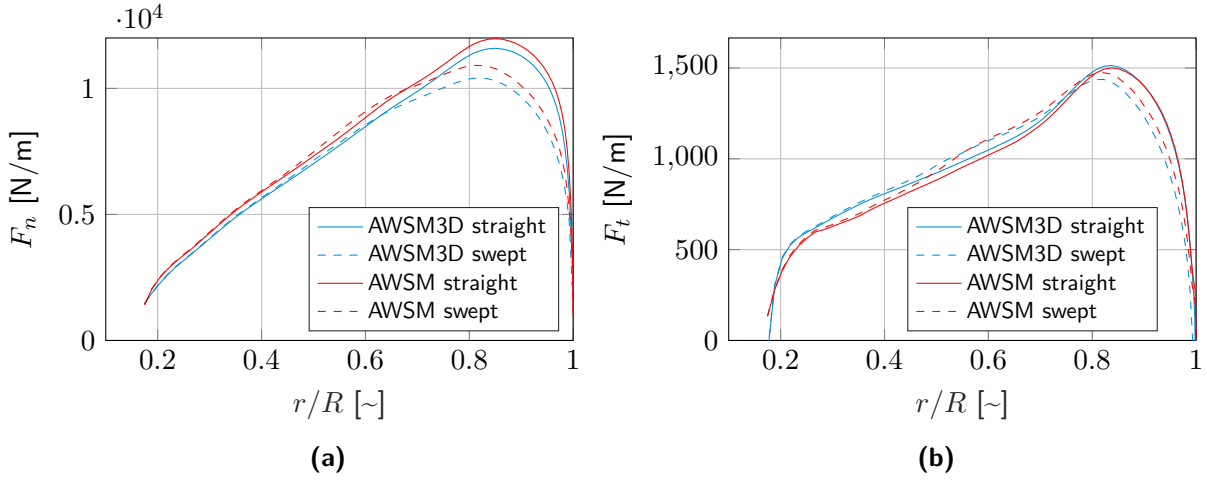

Figure 5-14: Chord-normal (a) and tangential (b) forces acting on baseline and fore swept IEA15MW turbine blade.

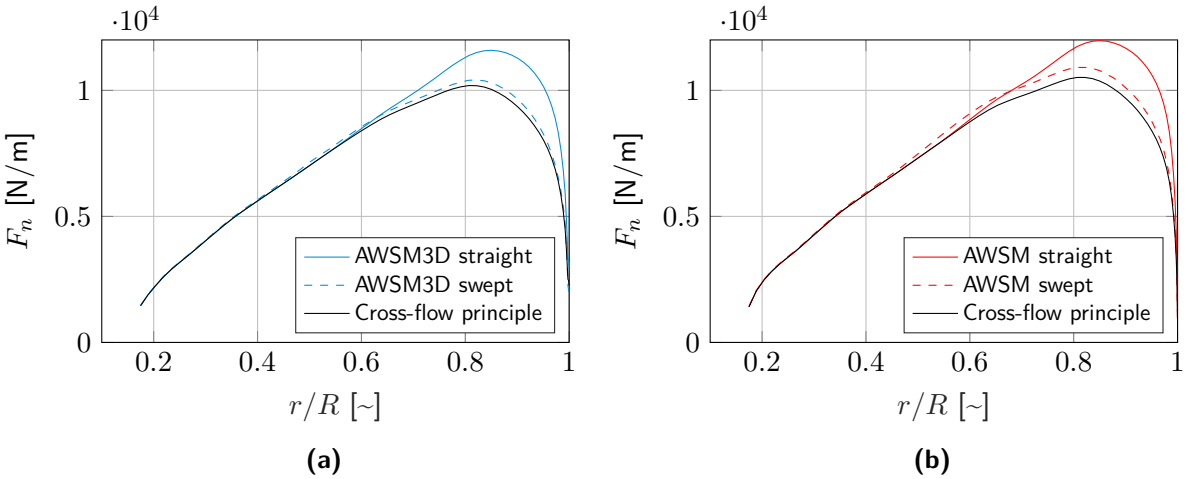

Figure 5-15: AWSM3D (a) and AWSM (b) chord-normal forces acting on baseline and fore swept IEA15MW turbine blade.

In order to decouple the 2D effect of sweep represented by the cross-flow principle, the simulation results are compared against their respective cross-flow correction curves in Figure 5-16. The AWSM curve appears to show a more drastic change shortly after sweep is introduced at $y_{start} = 0.5R$. Overall, in this case the AWSM curve does show a smaller decrease in force than the AWSM3D over the entire spanwise extent, compared to the aft swept case where the opposite held.

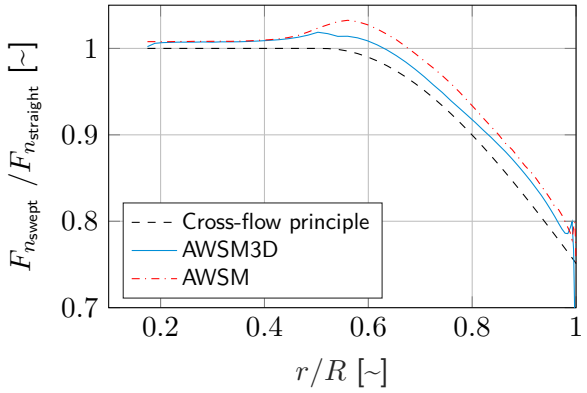

Figure 5-16: Fore swept blade chord-normal force fraction of straight configuration chord-normal force.

On the whole, a clear-cut distinction can be made between the 2D and 3D effects of sweep. As established earlier for the simple wing case, the cross-flow principle serves as an accurate representation of the 2D influence, denoted by a decrease in the aerodynamic load proportional to the cosine of the applied sweep angle. The 3D effect is primarily caused by the presence of the wake and manifests itself mainly through a spanwise load redistribution, although the latter is not convincingly proven in the fore swept turbine case. Assuming that the two effects are sufficiently independent such that these can be split apart and superimposed onto each other to form the final solution, a couple of conclusions can be drawn over the AWSM and AWSM3D results. The latter two show the same tendencies over the span but do vary in magnitude. For the more complex turbine case, the aft swept configuration presents a smaller drop in aerodynamic load for AWSM3D than AWSM, whereas in the fore swept case a smaller difference between the two is observed, with the AWSM results displaying a slightly smaller decrease in force.

Chapter 6

Conclusions and outlook

As of recent, wind turbine designs have reached past the 10 MW mark in energy production, largely owing to technological developments that allow for an increase in the rotor swept area. This has in turn led to the ever-growing necessity for more refined aerodynamic models. Particularly, given the large turbine radius and the ensuing large structural loads, it begs the question of whether aeroelastic phenomena may be turned to our advantage to favor energy production such that LCOE may be lowered.

One such method of inducing an aeroelastic effect is the application of blade sweep, which implies curving the blade in edgewise direction. The main premise is to couple the bending and twisting deformations in a manner in which passive load alleviation may be leveraged. The introduction of sweep has major implications for the aerodynamics of the blade, as both the inflow and the circulation system vary. To properly assess the effect of this modification, three models of varying fidelity levels are proposed for this study: BEM, lifting line, and panel method. This work, therefore, set out to investigate the underlying aerodynamic phenomena and assess the capabilities of the three models to capture and resolve these within the scope of potential flows.

The thesis work was performed in collaboration with TNO, which provided access to its AeroModule aerodynamics package. The latter contains a BEM and a lifting line model, called AWSM, both presented in a coalescent unified software module. This work engaged in the development of a panel method code aiming for a higher modeling fidelity level that is needed for conducting the proposed research. To provide a consistent comparison of the capabilities of the three models which minimizes the differences inherent to their respective implementation, it was decided that a panel code model would be developed as an extension of AeroModule.

Conceptual differences

The AWSM lifting line is based on the non-linear numerical adaptation of the classical lifting line theory, making use of airfoil polars to calculate local aerodynamic forces. These polars can be derived numerically or experimentally and ideally account for viscous flow properties. To compute the flow solution, an iterative scheme is used to balance the generated aerodynamic loading with the associated change in the induction system. These computations are evaluated at the quarter-chord position of each discretized station of the lifting line. A major limitation of lifting line theory is the assumption that the generated aerodynamic force is determined by the local velocity vector aligned with the plane of an airfoil section. This results in the cross-flow being neglected. Nonetheless,

simple sweep theory is used (also referred to as cross-flow principle), which asserts that whenever sweep is applied to a 2D geometry, the component of incoming flow parallel to the geometry may be ignored and therefore a correction factor which is a function of the sweep angle must be applied. The practical implementation of this in AWSM is to only consider the component of velocity normal to the lifting line in determining the resultant aerodynamic force.

Experiments have shown that the cross-flow theory is convincingly accurate in the case of bodies immersed in flows with predominantly 2D regimes. Although this does seem to be a reaffirmation of the insignificance of cross-flow, it is important to note that these cases explore the representation of cross-flow as a uniform flow that does not perturb the pressure field surrounding the bodies. However, this is not the case for 3D flows emerging around bodies with discontinuities or variation in circulation along the span, which give rise to trailing vorticity. In this case, the cross-flow is expected to play a role. AWSM includes a free vortex wake, which does model the effects of the skewed wake, but the influence of cross-flow is not captured. The BEM model on the other hand falls short of any of these capabilities and may require special correction factors to simulate such effects.

Panel method codes are deemed to be higher fidelity aerodynamic models for potential flows due to their more accurate representation of the flows around bodies. As opposed to lifting line models, these do not lump the circulation system in one point but rather distribute the singularity elements throughout the surface describing the body. The Laplace equation is solved by imposing the boundary conditions at multiple points per chordwise strip, which renders panel codes able to model the thickness and camber of more complex 3D shapes without the need to use airfoil data. The resulting solution may be used to determine the pressure field around the body, which includes the influence of cross-flow implicitly.

Panel code validation

The developed panel code, named AWSM3D, is based on an elementary source doublet method using constant strength elements. The surface is discretized into quadrilateral panels each housing a source and a doublet surface. The Dirichlet boundary condition is imposed at collocation points inside the body at each panel. To obtain the solution to the Laplace equation, the strength of the source terms is set equal to the normal component of the kinematic velocity at each panel. The free doublet wake formulation contained in AWSM is reused for AWSM3D with a few modifications. The wake is split into a part of the wake whose influence is fully accounted for in the boundary condition evaluation by taking its velocity potential, typically spanning over the latest few vortex panels shed, and a part further downstream whose influence is accounted for by imposing their induced velocity onto the kinematic velocity used to predefine the source strengths.

The panel code was validated for a series of cases varying in complexity. As such, AWSM3D was first validated against the analytical solutions for a circular cylinder, a van de Vooren airfoil in quasi-2D flow simulated by a very large AR, and a unit sphere. A sensitivity analysis was conducted to examine the influence of the choice of collocation point depth, which was revealed to be largely inconsequential, and a mesh convergence study reaffirmed the expected solution improvement given a grid refinement. An elliptical wing with a constant NACA0012 airfoil along the span was simulated, yielding adequate agreement with the analytical solution for an elliptical flat plate.

The quasi-2D NACA0018 rectangular wing case enabled the first direct comparison between the AWSM and AWSM3D models. Using inviscid airfoil polars generated with XFOIL, AWSM was shown to produce higher loads than AWSM3D. After supplying AWSM with quasi-2D polars generated with AWSM3D, the two models matched at the mid-section where cross-flow is absent. It was noted that the match deteriorated the closer to the tip region a section was, which is an indicator of the extent

of cross-flow caused by the tip vorticity. The panel code results showed a lift deficiency compared to the lifting line results in the presence of cross-flow.

The New MEXICO experiment dataset was used at last for validation [37]. Chordwise pressure distributions at five spanwise locations for three tip speed ratios, as simulated with AWSM3D, were compared against the corresponding measured data and the inviscid panel code developed by van Garrel [7]. The panel codes showed mostly good agreement against each other, except for locations where the difference in the mesh used was overriding. In a few notable instances, AWSM3D was shown to outperform van Garrel's model by showing better agreement with the experimental data where the flow regime was deemed to be closest to an inviscid flow, and therefore best resolved by panel code.

Analysis of sweep

Using a NACA0018 rectangular wing swept by a 45° angle with a very high aspect ratio, both AWSM and AWSM3D showed very good agreement with the cross-flow principle corrected curves in the mid-section region where the flow is fundamentally 2D. The correction factor was applied to each corresponding straight wing configuration result. However, the cross-flow correction accuracy wanes as the 3D phenomena start disturbing the flow closer to the tips. On the aft swept wing tip, the generated force was shown to be larger than the one predicted by the cross-flow principle. The opposite held for a fore swept wing. Despite the symmetry of the swept wing, the solution itself was not symmetrical with respect to the cross-flow corrected solution, with the lifting line solution exhibiting a larger degree of asymmetry. This comes as a result of the non-linear nature of the solution coupled with the influence of the skewed orientation of the wake.

The elementary mechanisms creating a load imbalance stem from the presence of a skewed wake. The orientation of the wake with respect to the wing creates less downwash on the aft end than on the fore end of the wing. The resulting induction system also affects the shape of the free wake. On the aft swept side the wake was pulled upstream, whereas on the fore end, the wake was dislocated further downstream than if a frozen wake would have been considered. Similarly, on the aft end the wake was subjected to more downwash. Additionally, the width of the skewed wake is reduced analogous to the aspect ratio.

The IEA 15-MW reference wind turbine [12] was also analyzed in swept configurations for normal wind turbine operating conditions. Again, the cross-flow adequately predicted the overall aerodynamic load deficiency when compared to the straight counterpart, while the tip region prediction was inadequate. A load redistribution was observed for the aft swept case, with the tip experiencing increased loads and the mid-section showing decreased loads compared to the cross-flow corrected curve. Although both the lifting line and the panel code display the same trends, the panel code appears to surpass the lifting line when compared to their respective cross-flow corrections. Analyzing the fore swept configuration, the cross-flow principle again adequately simulates the decrease in aerodynamic loading. In this case, no loading redistribution could be observed, with both models exhibiting less force decrease than the cross-flow theory predicted. This time around, AWSM showed larger loads than AWSM3D when compared to their respective cross-flow corrected curves.

Answer to research questions

1. **Is 2D blade element theory still valid for a swept blade, and what parameters limit the validity?**
   In the particular case of AWSM lifting line which uses 2D blade element theory to construct the aerodynamic solution, the implications of sweep are modeled with the help of the cross-flow principle. In a strictly 2D sense, this correction factor accurately resolves yawed inflow by

discarding any cross-flow component. The premise of such lifting line model is to resolve the aerodynamics at each spanwise station in a 2D manner and then recombine it within the 3D simulation as a whole. By coupling the body circulation with a wake, a load redistribution in spanwise direction ensues. It has been shown that although the larger scale effect of sweep is captured well, the regions of the flow where a 3D regime dominates exhibit a decline in solution accuracy. The problem is associated with the application of the cross-flow correction, initially derived for cross-flow modeled as a uniform flow field, which significantly misrepresents the distorted cross-flow. This is particularly visible close to the strong tip vorticity.

(a) ***What are the observed differences between the 3D panel surface simulation and the lifting line simulation?***
The AWSM3D panel code shows a lift deficiency for a straight wing compared to the AWSM lifting line which uses airfoil polars generated with XFOIL. This discrepancy was amended by reusing quasi-2D polars obtained with AWSM3D in AWSM, which then allowed for a solution match in the flow region where cross-flow was absent. As the cross-flows become more prominent in the vicinity of the tips, the discrepancy between the two models grows, with the panel code producing progressively less lift. Both models show good agreement in what concerns the large-scale effect of sweep. In the more complex wind turbine case, inconclusive results over the influence of sweep for the two models were obtained for the fore and aft swept blade. For a more in-depth analysis of these differences, refer to the section above.

(b) ***Can these differences be corrected at airfoil level?***
The cross-flow correction has proven to be an accurate 2D correction in flows with a predominantly 2D regime. By employing this correction locally and then reassembling the solution for the full 3D simulation domain, the AWSM lifting line has been shown to produce adequate results for swept geometries. Nonetheless, such a solution method fails to capture the smaller-scale local effect of the non-uniform cross-flow which is a characteristic of true 3D flows.

2. **What is sufficient validation of a 3D panel model for the swept blade configuration?**
The AWSM3D panel code approach for solving flows around swept bodies does not entail any special add-ons, given that cross-flows are implicitly part of the solution process. The fundamental check to bring panel codes up to par with lifting line codes in terms of accuracy is to verify the 2D solution for a swept wing, which is accurately modeled with the cross-flow principle theory. Subsequently, by including a wake circulation component, a panel code may be validated against a lifting line for finite bodies in regions with predominantly 2D flow regimes. As this represents the modeling ceiling for lifting line models, higher fidelity sources of validation need to be employed in regions with fundamentally 3D flows, such as CFD or experimental data, to model the smaller-scale implications of cross-flow.

Recommendations

The following section includes recommendations to address the limitations of the current work and suggest potential avenues to take it further. It is split into recommendations for future AWSM3D panel code enhancement and further research into the effect of wind turbine blade sweep.

Panel code development

The key learnings garnered from the entire development process of the AWSM3D panel code places this paper in a position to offer informed recommendations to guide future efforts and redirect attention to open issues. This chapter not only aims to address specific areas where enhancements

can be made but also provides a roadmap for future iterations and refinements. The recommendations should be viewed as a starting point, initiating a continuous cycle of improvement. The following non-exhaustive list of recommendations for further panel code development are proposed, in no particular order of importance.

1. Address issues related to the imposition of **Kutta condition around non-sharp trailing edges**. Particular attention is needed for the root region of turbine blades which conventionally have a circular root section smoothly transitioning into airfoils with a well-defined TE further outboard. The initial algorithm enforces the Kutta condition at any "trailing edge" it detects, although this automatic treatment is undesirable. For instance, placing an emission line along the typically cylindrical root of a turbine blade may result in imposing a non-physical condition on the flow. The current makeshift solution is to exclude regions with round "trailing edges".
2. In addition to the previous bullet point, adapt the panel code to include **non-sharp/blunt trailing edges**. In the current study, said blunt TEs were sharpened using a blending approach implemented in XFOIL, as detailed in subsection 5-2-1. Although not drastic, the pressure distribution has been shown to be distorted locally when using this method. The workaround may involve an algorithm change in the mesh generator and/or solution method.
3. Resolve issue related to the agglomeration of collocation points in the vicinity of a **very sharp (small TE angle) TE** or high resolution grid. Potential solutions for this have been identified in subsection 5-2-1.
4. Investigate **ground effect** modeling for panel code similar to LL implementation. AWSM incorporates ground effect via its Neumann formulation, whereas an equivalent Dirichlet formulation should be possible for the AWSM3D panel code. The AWSM simulations in this work were run far from ground level to minimize its effects. The generalized Kutta-Joukowsky theorem from Katz&Plotkin [5, 146-149], which takes ground effect into account, does not translate into any additional modeling elements for the panel code.
5. Validate the panel code for unsteady flows. Both the steady and the **unsteady Bernoulli equation** are implemented in separate subroutines in AWSM3D. In this work, only the steady formulation was used. The experimental dataset obtained by Piziali [44] for a pitching NACA0015 airfoil containing multiple oscillation amplitudes and frequencies may be used for panel code validation, although sparingly. To ensure a valid comparison, preferably test cases that steer clear of the airfoil's stall region such that the flow stays attached should be used. The analytical Theodorsen theory [45] may be later used for cross-checking.
6. A **triangular decomposition of surface panels** is included, however during the panel code validation, this method failed to generate the solution for the elliptical wing case. As per section 3-3-2, the triangular decomposition may be desired for its more accurate modeling of the body surface than the default quadrilateral representation at the expense of additional computational effort. This decomposition influences only the computation of the influence coefficient matrices, as the rest of the solution process carries on at the quadrilateral panel level.
7. Finalize **coupling to the structural solver** interface. AWSM3D followed suit from AWSM regarding the methodology of coupling the aerodynamic solver to the structural solver, hence most of the infrastructure is in place. The structural deformation input, which is specified for one point per spanwise station, may be used to redefine the perceived flow velocity at each collocation point on the mesh by including the influence of the heaving and pitching motions.
8. The **mesh generator** that was used to create the body meshes may be bundled or incorporated into the AeroModule. Further functionality may be added in addition to rectifying open issues and increasing its robustness and flexibility. The panel code strongly follows the indexing and the other specificities of the mesh generator in its functioning. The inclusion of said mesh generator into AeroModule may facilitate the coupling with the structural solver, in particular in view of the mesh deformation update per simulation time step.
9. The **tip treatment** algorithm for triangular patches closing up the surface needs to be refined.

The panel code allows placing triangular panels that are needed to close off the body mesh at extremities, although the recommended option is to cut such an extremity off. The issue stems from the lack of more sophisticated numerical schemes for determining the surface velocity in the vicinity of triangular patches and subsequent post-processing.

10. Investigate Katz&Plotkin **doublet induced velocity** for a constant quadrilateral element. AWSM3D uses the doublet quadrilateral – vortex ring equivalence to evaluate the velocity induced by a constant doublet quadrilateral panel. The equations derived in Katz&Plotkin have reportedly produced inconsistent results for this. Similarly, the quadrilateral source panel induced velocity also had to be altered from the equations presented in [5, chapter 10].
11. An investigation into the influence of the position of the **cut-off between the doublet and vortex wake** as per Figure 3-15, covered in section 3-3-2, may be conducted to verify whether the default doublet wake length of 4 panels is appropriate for the typical use of AWSM3D. Alternatively, the cut-off length may be determined at runtime given the geometry, the flow setup, and the ensuing prediction of the induction factor.
12. Explore the choice of the predefined **location of the shed vortex ring**. As per subsection 3-1-4, AWSM3D makes use of the same method of predefining the location of the first shed vortex ring in the wake as AWSM. Alternative methods, some of which are indicated in Figure 3-7, may model the shape of the wake more accurately.
13. Resolve the error encountered in subsection 5-1-1 for geometries swept by shearing. It is suspected that the **surface velocity** calculation should be refined by employing a method of averaging the gradients. Additionally, the definition of **reference dimensions** may need to be revised.
14. The AWSM3D **tower effect** implementation follows closely the method included in AWSM. However, the method would need to be adjusted for the Dirichlet boundary condition that is being solved in AWSM3D (as opposed to the Neumann BC in AWSM) before it can be used in the current version of AWSM3D. For this purpose, the wind turbine tower may be modelled as a solid thick non-lifting body, which is made possible with the introduction of the panel code.
15. **Wind distributions** other than "Simple" may need to be adapted for usage with the panel code if more sophisticated inflow models, some of which are included in the AeroModule package.
16. Explore the avenue of **plotting streamlines** using the panel code simulation results. The building blocks for this feature are already implemented in AWSM3D, as exemplified by the subroutine which evaluates the resulting flow velocity at a prescribed point in the computational domain.
17. Code acceleration by means of **parallelization** of the code may be improved upon. Most computationally expensive components of the code have already been transposed to their parallelized version using OpenMP®[46]. These mainly deal with the computation of the large influence coefficient matrices and induced velocities. Depending on the size, data structure and the algorithm itself, the parallel acceleration may be fine-tuned to improve performance. Benchmarking tools, such as commands to log the elapsed time per parallelized subroutine computation, are readily available in AWSM3D. Some subroutines have rudimentary acceleration algorithms in place that may benefit from further refining. For instance, the subroutine that calculates the velocity induced by the source quadrilateral elements in the wake has been shown to consume much more running time than other comparable computations.
18. In light of the previous point, the **influence of the source quadrilaterals onto the wake** may need to be critically assessed. The velocity induced by the source elements, which is a component of the wake roll-up, has been shown to be computationally highly expensive, especially for large wake sizes. Despite this, tests have shown that the resulting velocity component was nonetheless orders of magnitude smaller than other induced velocity components. A discussion may be held over the possibility of imposing a cut-off distance for the evaluation of the source influence over the wake.

19. **Large matrix algebra** lies at the core of most of the AWSM3D solution process, accounting for the majority of execution time. In its current implementation, a direct method for the matrix solution is used as parsed by the Intel® MKL optimized matrix library. Given the large size of these matrices, iterative methods for solving linear systems of equations may be preferred. The current method yields acceptable performance too, although there is room for improvement.

Further research

The following research recommendations are proposed to help generate more compelling arguments in favor of the conclusions derived in this work and continue

- A closer look at the streamlines in the vicinity of swept regions of the blade may reveal flow characteristics of interest in view of assessing the influence of cross-flow onto the aerodynamic solution. The current work sees the exclusion of the cross-flow component of the flow as being the main reason for the discrepancy identified between panel code and lifting line results, in particular close to the blade tip. The inclusion of cross-flow into the aerodynamic model appears to affect the aerodynamic solution in an opposing way for a fore and aft swept blade. Analyzing the tip streamlines may point out the extent to which cross-flow deviates from a uniform flow that is needed for cross-flow theory to accurately predict the lifting line solution. A conventional straight wing may serve as a good starting point for such an analysis.
- Further validation of simulation results for swept body geometries involving experimental measurement campaigns, such as the one in [47]. TU Delft is planning a similar measurement campaign for a rotating swept wind turbine blade. This would lead to more certainty over the accuracy of the AWSM3D panel code results for flows about swept geometries.
- Successfully coupling AWSM3D to a structural solver would allow for the assessment of sweep induced aeroelastic effects and subsequent analysis of the differences between the associated aerodynamic models of varying numerical fidelity. Sweep has primarily been devised for wind turbine blades to harness the potential of bend-twist coupling.

Bibliography

[1] K. Boorsma, F. Grasso, and J. Holierhoek, "Enhanced approach for simulation of rotor aerodynamic loads," Tech. Rep. ECN-M–12-003, ECN, 2012.

[2] S. Hoerner and H. Borst, *Fluid-dynamic Lift: Practical Information on Aerodynamic and Hydrodynamic Lift*. L.A. Hoerner, 1985.

[3] D. Kuchemann and J. Weber, *The subsonic flow past swept wings at zero lift without and with body*. HM Stationery Office, 1953.

[4] S. Larwood, C. van Dam, and D. Schow, "Design studies of swept wind turbine blades," *Renewable Energy*, vol. 71, pp. 563–571, 2014.

[5] J. Katz and A. Plotkin, *Low-Speed Aerodynamics*. Cambridge Aerospace Series, Cambridge University Press, 2 ed., 2001.

[6] K. Dixon, "The Near Wake Structure of a Vertical Axis Wind Turbine," Master's thesis, TU Delft, 2008.

[7] A. van Garrel, *Multilevel panel method for wind turbine rotor flow simulations*. PhD thesis, University of Twente, 2016.

[8] G. Bernardini, J. Serafini, M. Molica Colella, and M. Gennaretti, "Analysis of a structural-aerodynamic fully-coupled formulation for aeroelastic response of rotorcraft," *Aerospace Science and Technology*, vol. 29, no. 1, pp. 175–184, 2013.

[9] J. H. Baayen, "Vortexje - An Open-Source Panel Method for Co-Simulation," *CoRR*, vol. abs/1210.6956, 2012.

[10] A. van Garrel, "Development of a Wind Turbine Rotor Flow Panel Method," Tech. Rep. ECN-E–11-071, ECN, 12 2011.

[11] J. Anderson, *Fundamentals of Aerodynamics*. New York, United States: McGraw Hill Education, 6th international ed., 2017.

[12] E. Gaertner, J. Rinker, L. Sethuraman, F. Zahle, B. Anderson, G. Barter, N. Abbas, F. Meng, P. Bortolotti, W. Skrzypinski, G. Scott, R. Feil, H. Bredmose, K. Dykes, M. Sheilds, C. Allen, and A. Viselli, "Definition of the IEA 15-Megawatt Offshore Reference Wind Turbine," tech. rep., International Energy Agency, 2020.

[13] S. Hoerner, *Fluid-dynamic Drag: Practical Information on Aerodynamic Drag and Hydrodynamic Resistance*. Hoerner Fluid Dynamics, 1965.

[14] R. Vos and S. Farokhi, *Introduction to transonic aerodynamics*, vol. 110. Springer, 2015.

[15] C. Harper, R. Maki, A. R. Center, U. S. N. Aeronautics, and S. Administration, *A Review of the Stall Characteristics of Swept Wings*. NASA TN D, National Aeronautics and Space Administration, 1964.

[16] B. S. Liebst, "Wind turbine gust load alleviation utilizing curved blades," *Journal of Propulsion and Power vol. 2 iss. 4*, vol. 2, jul 1986.

[17] M. Zuteck, "Adaptive Blade Concept Assessment: Curved Planform Induced Twist Investigation," Tech. Rep. SAND2002-2996, 2002.

[18] T. Ashwill, "Parametric Study for Large Wind Turbine Blades: WindPACT Blade System Design Studies," 8 2002.

[19] S. Larwood and M. Zuteck, "Swept Wind Turbine Blade Aeroelastic Modeling for Loads and Dynamic Behavior," *AWEA Windpower*, 01 2006.

[20] T. Ashwill, G. Kanaby, K. Jackson, and M. Zuteck, "Development of the Swept Twist Adaptive Rotor (STAR) Blade," 01 2010.

[21] J. Chattot, "Effects of Blade Tip Modifications on Wind Turbine Performance Using Vortex Model," *46th AIAA Aerospace Sciences Meeting and Exhibit*, 01 2008.

[22] M. Hand, D. Simms, L. Fingersh, D. Jager, J. Cotrell, S. Schreck, and S. Larwood, "Unsteady Aerodynamics Experiment Phase VI: Wind Tunnel Test Configurations and Available Data Campaigns," 01 2001.

[23] K. Suzuki, S. Schmitz, and J. Chattot, "Analysis of a swept wind turbine blade using a hybrid navier-stokes/vortex- panel model," in *Computational Fluid Dynamics 2010 - Proceedings of the 6th International Conference on Computational Fluid Dynamics, ICCFD 2010*, (Netherlands), pp. 213–218, Kluwer Academic Publishers, 2011.

[24] D. Verelst and T. Larsen, *Load Consequences when Sweeping Blades - A Case Study of a 5 MW Pitch Controlled Wind Turbine*. No. 1724(EN) in Denmark. Forskningscenter Risoe. Risoe-R, Danmarks Tekniske Universitet, Risø Nationallaboratoriet for Bæredygtig Energi, 2010.

[25] J. Jonkman, S. Butterfield, W. Musial, and G. Scott, "Definition of a 5-MW Reference Wind Turbine for Offshore System Development," 2 2009.

[26] N. Picot, D. Verelst, and T. Larsen, "Free yawing stall-controlled downwind wind turbine with swept blades and coned rotor," *European Wind Energy Conference and Exhibition 2011, EWEC 2011*, 01 2011.

[27] D. Griffin, "WindPACT Turbine Design Scaling Studies Technical Area 1-Composite Blades for 80- to 120-Meter Rotor," 4 2001.

[28] A. Li, G. Pirrung, H. A. Madsen, M. Gaunaa, and F. Zahle, "Fast trailed and bound vorticity modeling of swept wind turbine blades," vol. 1037, jun 2018.

[29] J. Hess and A. Smith, "Calculation of potential flow about arbitrary bodies," *Progress in Aerospace Sciences*, vol. 8, pp. 1–138, 1967.

[30] M. Gennaretti and G. Bernardini, "Novel Boundary Integral Formulation for Blade-Vortex Interaction Aerodynamics of Helicopter Rotors," *AIAA Journal*, vol. 45, no. 6, pp. 1169–1176, 2007.

[31] B. Maskew, "VSAERO: A computer program for calculating the non-linear aerodynamic characteristics of arbitrary configurations : user's manual," tech. rep., Ames Research Center, United States, National Aeronautics and Space Administration, 1982.

[32] L. Dragos, *Mathematical Methods in Aerodynamics*. Springer, 2003.

[33] C. Geuzaine and J.-F. Remacle, "Gmsh reference manual version 4.11.1." https://gmsh.info/doc/texinfo/gmsh.html. Accessed: 02-03-2023.

[34] C. Geuzaine and J.-F. Remacle, "Gmsh: A 3-D finite element mesh generator with built-in pre-and post-processing facilities," *International journal for numerical methods in engineering*, vol. 79, no. 11, pp. 1309–1331, 2009.

[35] M. Drela, "XFOIL: An Analysis and Design System for Low Reynolds Number Airfoils," in *Low Reynolds Number Aerodynamics* (T. J. Mueller, ed.), (Berlin, Heidelberg), pp. 1–12, Springer Berlin Heidelberg, 1989.

[36] M. Hepperle, "JAVAFOIL Users Guide," tech. rep., 2011.

[37] J. Schepers and H. Snel, "MEXICO, Model experiments in controlled conditions," Tech. Rep. ECNE-07-042, ECN, 2007.

[38] K. Boorsma and J. Schepers, "New MEXICO experiment Preliminary Overview with Initial Validation," Tech. Rep. ECN-E–14-048, ECN, 2014.

[39] E. K. Fritz, C. Ferreira, and K. Boorsma, "An efficient blade sweep correction model for blade element momentum theory," *Wind Energy*, vol. 25, no. 12, pp. 1977–1994, 2022.

[40] L. Morino and C.-C. Kuo, "Subsonic potential aerodynamics for complex configurations: A general theory," *AIAA Journal*, vol. 12, no. 2, p. 191 197, 1974.

[41] J. M. E. Navarro, *Panel method for the aerodynamic calculation of mixed configurations with finite thickness and zero thickness*. PhD thesis, Universidad Politécnica de Madrid, 2017.

[42] S. Yon, J. Katz, and A. Plotkin, "Effect of airfoil (trailing-edge) thickness on the numerical solution of panel methods based on the Dirichlet boundary condition," *AIAA Journal*, vol. 30, no. 3, pp. 697–702, 1992.

[43] J. Schepers, K. Boorsma, T. Cho, S. Gomez-Iradi, A. Schaffarczyk, A. Jeromin, W. Z. Shen, T. Lutz, K. Meister, B. Stoevesandt, S. Schreck, D. Micallef, R. Pereira, T. Sant, H. Madsen, and N. Sørensen, "Final report of IEA Task 29, Mexnext (phase 1): analysis of MEXICO wind tunnel measurements," *Wind Energy*, vol. 2013, 05 2014.

[44] R. Piziali, "2-d and 3-d oscillating wing aerodynamics for a range of angles of attack including stall," Tech. Rep. NASA-TM-4632, 1994.

[45] T. Theodorsen, "General theory of aerodynamic instability and the mechanism of flutter," Tech. Rep. NACA-TR-496, National Advisory Committee for Aeronautics, 1949.

[46] L. Dagum and R. Menon, "OpenMP: an industry standard API for shared-memory programming," *Computational Science & Engineering, IEEE*, vol. 5, no. 1, pp. 46–55, 1998.

[47] T. Barlas, G. R. Pirrung, N. Ramos-García, S. González Horcas, A. Li, and H. A. Madsen, "Atmospheric rotating rig testing of a swept blade tip and comparison with multi-fidelity aeroelastic simulations," *Wind Energy Science*, vol. 7, no. 5, pp. 1957–1973, 2022.

Glossary

List of Acronyms

ADAMS	Automated Dynamic Analysis of Mechanical Systems
AR	Aspect Ratio
AWSM	Aerodynamic Windturbine Simulation Module
BEM	Blade Element Momentum
BC	Boundary Condition
CFD	Computational Fluid Dynamics
DNW	German-Dutch Wind Tunnels
ECN	Energy research Centre of the Netherlands
FAST	Fatigue, Aerodynamics, Structures, and Turbulence
HAWC2	Horizontal Axis Wind turbine simulation Code 2nd generation
HAWT	Horizontal Axis Wind Turbine
IEA	International Energy Agency
IEC	International Electrotechnical Commission
LCOE	Levelized Cost of Electricity
LL	Lifting Line
MIT	Massachusetts Institute of Technology
MKL	Math Kernel Library
MLMIC	Multi-Level Multi-Integration Cluster
MSC	MacNeal-Schwendler Corporation
NACA	National Advisory Committee for Aeronautics
NREL	National Renewable Energy Laboratory
RPM	Revolutions Per Minute

STAR	Sweep Twist Adaptive Rotor
TE	Trailing Edge
TNO	Netherlands Organisation for Applied Scientific Research
TUD	Delft University of Technology
VSAERO	Vortex Separation AEROdynamics
2D	Two-Dimensional
3D	Three-Dimensional

Chapter 2

α	Angle of attack
γ	Power law exponent
λ	Sweep angle
c	Chord length
c_p	Pressure coefficient
d	Displacement
L_{Blade}	Blade length
L	Lift force
t	Thickness
u, v, w	Cartesian velocity components
x, y, z	Cartesian coordinates

Chapter 3

α	Angle of attack
β	Angular coordinate
Γ	Vortex strength
Γ	Circulation
μ	Doublet strength
ρ	Density
σ	Source strength
$\vec{\tau}$	Tangential vector
Φ	Velocity potential
Ω	Angular velocity
c	Chord length
c_p	Pressure coefficient
$\hat{d}$	Differentiation direction vector
$\vec{F}$	Force vector
i, j, k	Index numbers
$\vec{n}$	Normal vector
$\mathbf{n}$	Normal vector
N	Number of elements

p	Pressure
$\mathbf{Q}_\infty$	Onset flow velocity vector
$\mathbf{r}$	Position vector
r	Radius
S	Surface
t	Time
$\vec{u}$	Velocity vector
$\mathbf{u}$	Position vector (spherical)
u	Velocity magnitude
u_i	Velocity component
$\vec{v}$	Contour velocity normal vector
$\mathbf{v}$	Relative velocity vector
V	Volume
V	Flow velocity
x	Chord line coordinate

Chapter 4

Γ	Circulation
θ	Angular coordinate
λ	Tip speed ratio
A, B, D, l	van de Vooren airfoil parameters
b	Wingspan
c	Chord length
c_l	Sectional lift coefficient
c_p	Pressure coefficient
r	Radius (position)
R	Radius
u_r, u_θ	Polar velocity components
U_∞, u_∞	Inflow velocity
u, v, w	Cartesian velocity components
x, y, z	Cartesian coordinates

Chapter 5

α	Angle of attack
γ	Power law exponent
Γ	Circulation
λ	Sweep angle
b	Wingspan
c	Chord length
c_l	Sectional lift coefficient
c_p	Pressure coefficient
F_{ax}	Axial force to rotor plane
F_n	Chord-normal force
F_t	Chord-tangential force
F_{tan}	Tangential force to rotor plane
t	Thickness

U_∞	Inflow velocity
x, z	Cartesian coordinates